Gas-liquid flow regimes in a novel rocking and rolling flow loop

Madina Naukanova, Gianluca Lavalle, Jérôme Douzet, Ana Cameirao, Jean-Michel Herri

Graphical Abstract

Gas-liquid flow regimes in a novel rocking and rolling flow loop

Madina Naukanova, Gianluca Lavalle, Jérôme Douzet, Ana Cameirão, Jean-Michel Herri

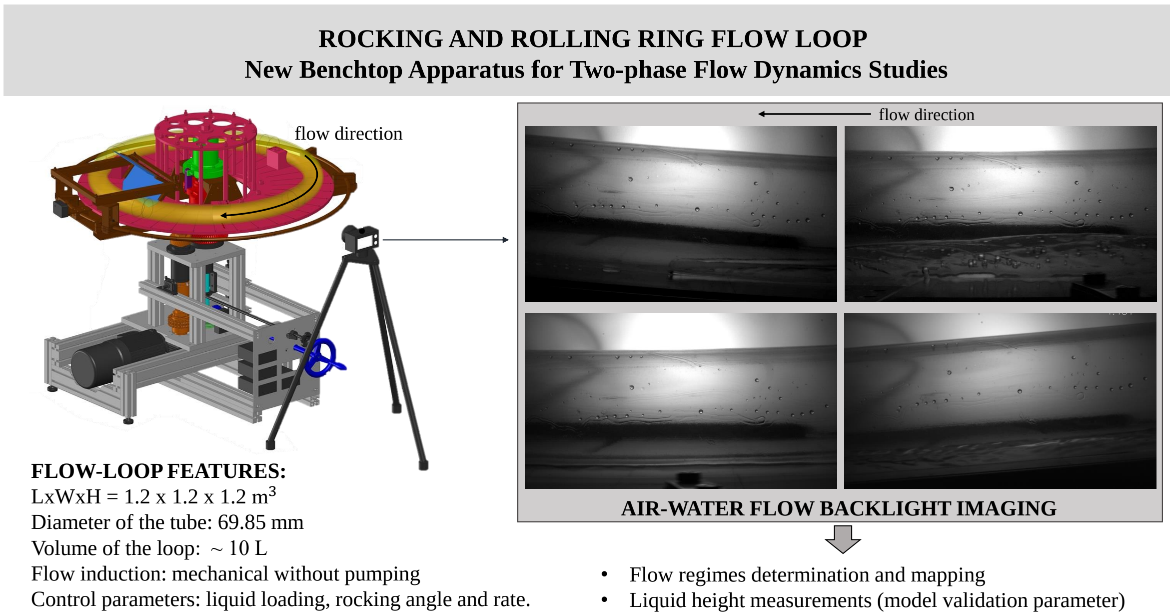

Highlights

Gas-liquid flow regimes in a novel rocking and rolling flow loop

Madina Naukanova, Gianluca Lavalle, Jérôme Douzet, Ana Cameirão, Jean-Michel Herri

- A novel flow-testing benchtop without pumping is designed.
- Backlight imaging is adopted to characterize flow behaviour.
- The influence of centrifugal force on flow regimes and flow transitions are analysed.
- Energy minimization, mechanistic and combined models are applied to predict the flow.

Gas-liquid flow regimes in a novel rocking and rolling flow loop

Madina Naukanova[a,*], Gianluca Lavalle[a], Jérôme Douzet[a], Ana Cameirão[a], Jean-Michel Herri[a]

[a] *Mines Saint-Etienne Univ Lyon CNRS UMR 5307 LGF Centre SPIN F - 42023 Saint-Etienne France*

Abstract

Predicting two-phase flow pattern characteristics and flow transition is fundamental to address several industrial problems, *e.g.* for the oil and gas industry. In order to fulfill the upscaling from the laboratory to the industrial scale, resource-efficient flow testing facilities which closely replicate industrial flow characteristics are needed. To address this, we introduce a new experimental device named as the Rocking and Rolling Ring Flow Loop (3RFL), which is size, cost, and time-efficient. In the present work, we employ the 3RFL apparatus at atmospheric pressure and temperature, with air and water as working fluids. However, the ultimate goal of our work is to build an experimental set-up capable of capturing the under-pressure reactive multiphase flow (gas-liquid-solid) dynamics typical of flow assurance in oil production and transportation. At the moment, the 3RFL can induce different flow regimes by adjusting the system control parameters such as rocking angle, rocking rate, and liquid volume fraction, all without requiring a pump. We observe three flow regimes, and analyze the impact of control parameters on their emergence. Our findings reveal that flow regime transitions are influenced by the competition between gravitational and centrifugal forces, which arise due to the curvature of the tube. Among three employed modeling strategies, namely mechanistic modeling, total energy minimization and a combined approach, we find that the total energy minimization model best compares to the experimental liquid height.

*Corresponding author

Email address: naukanovamadina@gmail.com (Madina Naukanova)

Keywords: Ring flow loop, Gas-liquid flow, Flow regime prediction, Backlight imaging, Energy minimization model

1. Introduction

Gas-liquid flow transport is a common occurrence in various industrial processes, and it becomes particularly challenging in oil and gas flowlines. The extraction of oil can lead to the formation of gas hydrates, which are ice-like crystals resulting from the entrapment of light hydrocarbon molecules in the water lattice structure (Sum et al., 2009; Balakin, 2010). These gas hydrates pose significant financial and safety risks since they are adhesive and, therefore tend to agglomerate and stick to the pipe wall, and finally block the flow (Kinnari et al., 2008; De Almeida et al., 2023). Traditional solutions for this problem are based on the avoidance of hydrate formation, which is achieved by injection of environmentally harmful chemical additives in large quantities. Today, the acceptance strategy proposes the use of anti-agglomerants to mitigate particle adhesion and thereby enable flow transportation along with hydrates (Kinnari et al., 2015). However, this strategy is based on the co-existence of gas/liquid phases along with the solid phase, for which a strong interplay is expected. Melchuna (2016) reported that the gas-liquid flow influences the kinetics of hydrate growth and, consequently, the crystal size and location. De Almeida et al. (2023) showed that the water-cut, *i.e.* the volume of water in oil, strongly influences the hydrate onset formation and the plugging risk. Conversely, hydrates intrinsically consume water, therefore flow characteristics change. For instance, at 50% water-cut, hydrate formation might lead to a change in the continuous carrying phase (from oil in water to water in oil). As such, successful implementation of hydrate management strategies requires a deep knowledge of two-way coupling between hydrate formation and multiphase flow characteristics, *e.g.* pressure drop, liquid holdup and flow regime.

Nowadays, there is a wide range of experimental apparatus dedicated to studying hydrate crystallization and transport. The key criteria that apparatus must meet when studying flow-dependent phenomena of hydrate formation are the ability to reproduce flow regimes and to control flow variables, providing interpretative experimental data along with flow visualization. Although pilot-scale flow loops meet most of these requirements, they have drawbacks such as high investment, reduced cooling capacity and large required time to conduct test campaigns. To facilitate time and cost-efficient laboratory testing coupled with modelling procedures, benchtop testing systems are needed. Examples of benchtop apparatus are Rock Flow Cell (RFC) (Sa et al., 2019) and Euler Wheel (Kelland et al., 2015). The RFC is made up of an o-ring-sealed straight pipe (less than 1 meter long) with a diameter of a few centimeters mounted on a horizontal mobile table which tilts back and forth by an electric motor at a controlled rate and angle. Thus, unlike in pilot-scale flow loops, the gravitational force acting downward drives fluid flow, eliminating the influence of the pump on particle flow. Flow visualization in the RFC system is afforded by two windows located at both ends of the pipe. By varying the liquid loading, rocking angle and rate, the RFC can readily replicate various flow regimes, such as stratified, stratified-wavy, slug, and dispersed bubble. This allows one to comprehend the flow-dependent phenomena of hydrate formation. Other benefits of the RFC are low capital and operational expenses, short test times and repeatability of the results. Moreover, the compactness of the RFC opens up the possibility of applying computational fluid dynamics (CFD). However, the flow in the RFC often changes direction due to collisions with the ends of the tubes, which leads to a disturbance of the flow.

The Euler wheel consists of a narrow pipe (whose diameter is smaller than 30 mm) coiled to form a wheel mounted on a horizontal disc. Flow circulation is initiated by the rotation of a spherical ball along the wheel. Such kinematics permits reproducing pipeline flow. The maximum velocity of the fluid reaches 1.2 m/s (Kelland et al., 2015). The onset of hydrate formation can be detected by monitoring the pressure of the system and by visual observations. Same as for the RFC, the Euler wheel allows time and cost-efficient testing without a pump. However, the reproduction of flow regimes, such as those observed in flow lines, is hard to achieve as the ratio of the tube length to the diameter is small (~ 10).

To eliminate these shortcomings, we present a new experimental apparatus that can generate flow velocities approaching those of the industrial fields and different pipeline flow regimes. This apparatus is dubbed Rocking and Rolling Ring Flow Loop (3RFL) and has been designed and assembled at Mines Saint-Etienne. It consists of a transparent cellulose acetyl butyrate ring loop ($d = 69.85$ mm, $D = 840$ mm) installed on a horizontal mobile platform. This platform rolls sequentially by four sides, *i.e.* to the right, front, left, and back, driven by an electrical motor. Compared to the RFC, in the 3RFL additional "rolling" motion over the y-axis is added (Fig. 1). This resulted in a smoother flow resembling a flowline. The transparency of

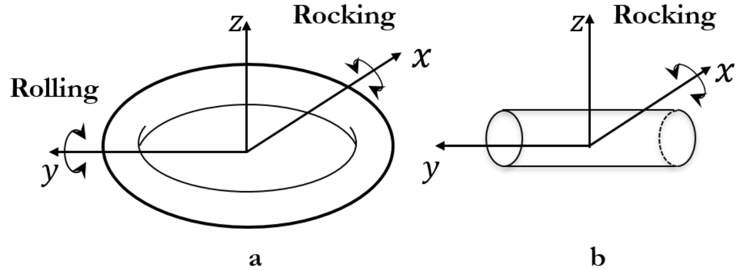

Figure 1: Sketch of the kinematics of the rocking-based types of experimental apparatus: (a) rocking and rolling ring flow loop (this work) and (b) Rock Flow Cell (Sa et al., 2019).

the loop allowed us to apply backlight imaging tomography to characterize the flow.

The ultimate aim of our work is to build an experimental set-up capable of capturing the reactive multiphase flow (gas-liquid-solid) dynamics typical of flow assurance issues. In particular, we are interested in the hydrate formation and in the interplay between crystallization and fluid flow. Methane hydrates form under particular conditions of pressure and temperature ($P > 80$ bar and $T < 4°$). In the last 30 years, several studies have been done in the SPIN centre at Mines Saint-Etienne to experimentally characterize, in batch reactors and pipe reactors, the hydrate formation for flow assurance. The main outcome is the Archimede flow loop (Fidel-Dufour et al., 2005; Melchuna, 2016; Herri et al., 2017; Pham et al., 2020; De Almeida et al., 2023): a multi-instrumental 50-meter long flow loop capturing the hydrate formation under water-oil-gas flow. However, in the Archimede flow loop, the gas phase is solely dissolved into the liquid, resulting in the impossibility to observe typical flow patterns of flow assurance, such as gas-liquid stratified, slug flow or annular flow. Also, visualisation of the flow is only possible via a small (a few centimeter long) window. These issues have prompted us to build the 3RFL apparatus with the aim to have a small-scale set-up with transparent tubes allowing us to observe a larger range of flow patterns. However, the step-by-step development strategy of the 3RFL system is similar to what we have pursued for the Archimede flow loop. Firstly, the loop is employed at ambient pressure and temperature, with air and water as working fluids. This is the study introduced in the present work. Secondly, the loop will be operated at conditions closer to those of the oil production and transport (oil-water-methane flows under high pressure and low temperature) and equipped with more advanced experimental techniques qualified to work under high pressures and low temperatures. This study will be addressed in future works.

Nonetheless, the 3RFL has certain constraints, including the complexity of handling very high liquid volume fractions, as the system strongly relies on liquid motion, and dry-out which is challenging to model. Also, reproducing annular flow within the 3RFL is not possible. Indeed, annular flow occurs when the gas velocity is significantly higher than the liquid velocity, as the gas flow generates liquid atomization leading to the formation of droplet touching the upper wall and forming a liquid film. In our system the gas phase is simply driven by the shear exerted by the liquid flow, limiting the gas velocity to relative low values. In addition, flow in curved tubes is more complex in nature than flow in straight tubes. As reported by Eustice (1911) and Dean (1927), who studied single-phase flow, the complexity lies in the effect of tube curvature-induced centrifugal force which develops a secondary flow leading to active radial mixing. It is possible to imagine that adding a supplementary phase, such as oil, would add yet another layer of complexity to the flow behaviour.

Given the difficulties and the challenges that we might face in fully characterizing - by means of experiments - such a complex multiphase flow, we complement the experimental work presented herein with modeling development, which in turns is helpful to study the effect of varying fluid properties and flow conditions, *e.g.* replacing water with oil. In particular, we employ three different modeling approaches: mechanistic model, total energy minimization model and a hybrid model built by combining the previous two strategies. As for the 3RFL system, also in the modeling development we adopt a step-by-step strategy. Firstly, we consider a simple 1D model neglecting curvature effects, de-wetting and wavy gas-liquid interface. This is introduced in the present study. In future works, the model will be upgraded to take into account those effects, in addition to a third phase (oil), pressure and temperature effects and hydrate kinetics of crystallization.

Both the mechanistic and the total energy minimization approaches are usually employed to characterize gas-liquid flows in pipelines. Analytical models have been developed since the early work of Taitel and Dukler (1976a). The authors established a mechanistic model to predict five basic flow patterns, such as stratified smooth, stratified wavy, annular, intermittent and dispersed bubbles. More importantly, their model takes into consideration many factors that affect flow configuration, including geometrical parameters, *e.g.* pipe diameter and inclination angle, physical parameters, *e.g.* density and viscosity of phases and operational parameters, *e.g.* two-phase flow rates. However, mechanistic models employ closure relationships for wall and interfacial shear stresses. Following Taitel and Dukler (1976a), many different friction factor expressions have been established to describe the closure relations at the interface (Amaravadi, 1994; Ouyang and Aziz, 1996; Xiao et al., 1990; Garcıa et al., 2003). However, they remain to be empirical and different from one study to another. An important limitation of mechanistic models is that multiple solutions might exist in terms of equilibrium liquid height h_L for the same flow configurations. This was highlighted by several studies (Landman, 1991; Taitel and Barnea, 1990; Barnea and Taitel, 1992, 1994; Ullmann et al., 2003; Thibault et al., 2015).

More recently, other modeling strategies have been developed to overcome the problem of closure relations at the interface typical of mechanistic models. Chakrabarti et al. (2005) have been the first to use the energy minimization approach to estimate two-phase flow parameters such as liquid holdup and pressure gradient for two-phase flow. It has been assumed that the system would stabilize to its minimum energy, while the pressure gradient in both phases would be the same. The steady state, stratified liquid-liquid horizontal flow with a flat interface has been considered in their study. After Chakrabarti et al. (2005), the total energy minimization approach found its continuation in the work of Sharma et al. (2011). Sharma et al. (2011) applied the total energy minimization model to predict five flow patterns for horizontal and near horizontal oil-water flows. Lee et al. (2013) have been the first to employ the energy minimization concept to predict gas-liquid stratified flow characteristics. The authors considered gas-liquid flow as a dissipative process and that the structure of the gas-liquid flow must be the one that minimizes the dissipated energy within a control volume of a pipe. Assuming a flat interface between phases, continuity of pressure gradients in both phases and constant velocity profiles, the authors suggested that the minimum dissipated energy corresponds to the minimum pressure gradient. The pressure gradient of the system has been expressed as a sum of gas and liquid phases' momentum conservation equations, such that the final equation is released from the interfacial shear stress component (Lee et al., 2013).

To conclude, the aim of our work is to overcome the above-mentioned shortcomings of compact apparatus, such as Rock Flow Cell and Euler wheel, and pilot-scale apparatus, as the Archimede flow loop developed in the last decades at Mines Saint-Etienne. For this, we introduce here a novel flow loop, whose rocking and rolling motion promotes the occurrence of flow patterns under typical hydrodynamic conditions of flow assurance problems. We leave to future studies the improvements of such a flow loop to account for thermodynamics conditions fostering hydrate formation. Meanwhile, we compare the experimentally observed liquid heights to the predictions of three different modeling strategies, of which one is a novel hybrid approach developed by combining mechanistic and total energy minimization modeling.

The article is structured as follows. Section 2 presents details on the flow testing procedure, including an extensive description of the experimental apparatus, flow visualization elements, system control parameters, and flow testing procedure. Section 3 discusses the observed flow characteristics, such as flow regimes, flow regime transitions, and liquid height, depending on the control parameters of the flow. Further, section 4 describes three modeling approaches applied for predicting the liquid height of the studied flow and compares the obtained predictions against experimental results. Finally, in section 5 key outcomes are summarized.

2. Methodology

2.1. Description of experimental setup

The Rocking and Rolling Ring Flow Loop (3RFL), illustrated in Fig. 2, measures 1.2 meters in height, width, and length. The apparatus base is constructed using aluminium blocks (in grey). The 3RFL consists of a transparent ring loop (G in Fig. 2) installed on a horizontal mobile platform. As the name of the apparatus suggests, the “rocking and rolling” characterizes the nature of the mechanical motion of the platform while the ”ring” identifies the flow testing loop geometry. The platform itself is a circular acrylic disc with a diameter of $D = 0.96 \quad m$, featuring a circular cut-out in the centre. This platform is attached to a metal hood (E in Fig. 2), which in turn is mounted on the slave rotor (B in Fig. 2). The platform, driven by mechanical motion, tilts sequentially by four sides, *i.e.* to the right, front, left, and back. In this way, controlled flow within the loop is induced. To have a better idea of how this device works, please refer to Video 1 in the supplementary materials. Two parameters drive the ring loop: the rocking angle (θ) measured in degrees and the rocking rate (f_R) measured in oscillations per minute (opm). Note that one oscillation per minute of the ring loop corresponds to one revolution per minute (rpm) of the rotating central shaft,

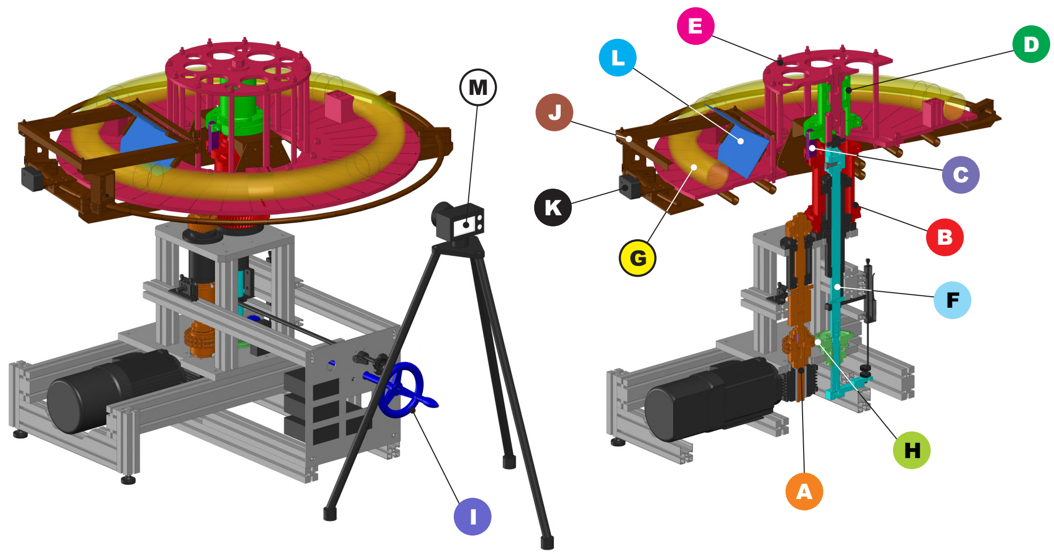

Figure 2: Sketch of the Rock&Roll Ring Flow Loop (3RFL) and main elements. A: Driveshaft / B: Rotor / C: Connecting rod / D: Slave rotor / E: Metal disc / F: Central shaft / G: Torus tube / H: Turning nut / I: Hand wheel shaft / J: Rotary arm (and linked parts) / K: Action camera / L: Mirrors / M: High-speed camera.

to be introduced later. Other control parameters of the system are the liquid volume fraction and the ring loop dimensions, *e.g.* diameters of the tube (d) and of the ring (D). In Table 1 limits of variation of control parameters and the possibility of their modification while operating are given.

The apparatus is equipped with a temperature probe, displacement (to adjust θ), and inductive sensors (to adjust f_R). To facilitate air-water flow observations, two different cameras were used - specifically, action and high-speed cameras (labelled as K and M respectively in Fig. 2). The action camera was employed along with a mirror system (L in Fig. 2). There are two types of mirror systems, one is entitled to project the top view, and another is the back view of the flow. The system of mirrors and the action camera are mounted on the rotary arm (J in Fig. 2) and therefore rotate about the central axis of the 3RFL following the flow. The action camera (GoPro Black Hero 9) and mirrors are arranged in such a way that the video captures both a side view of the tube and a top (or back) view, which is projected through the mirror (see Video 5 in supplementary materials). Meanwhile, the high-speed monochromatic camera was combined with backlighting. The high-speed

Control Parameters	Notation	Unit	Range	Adjustable during the test
Rocking rate	f_R	opm	3-36.2	Yes
Inclination angle	θ	$^\circ$	0-45	Yes
Diameter of the ring	D	mm	500-900	No
Diameter of the tube	d	mm	6 - 80	No
Liquid volume fraction	φ_L	$-$	0-1	No

Table 1: Control parameters of the 3RFL apparatus and their range of variations as well as the potential for their change during the test.

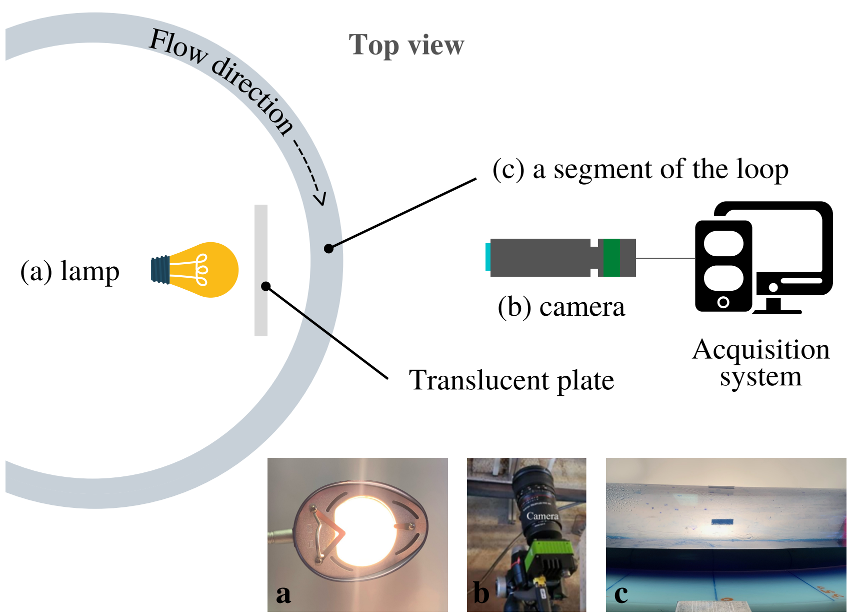

Figure 3: A sketch of air-water flow backlight imaging with a high-speed camera.

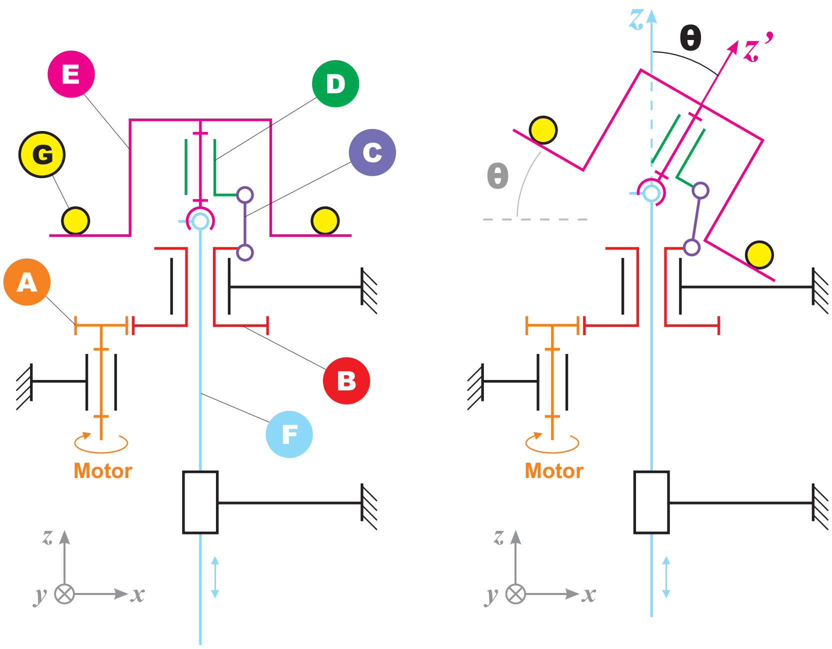

Figure 4: A simplified kinematic diagram illustrates the positions of assemblies of the 3RFL at the horizontal and inclined cases. A: Driveshaft / B: Rotor / C: Connecting rod / D: Slave rotor / E: platform / F: Central shaft / G: Torus tube.

camera is aligned with the centre line of the ring loop and positioned at a distance of 1 m from the outer side of the tube, while the light source is placed behind the tube as illustrated in Fig. 3. Given that the action camera is rotating around the ring loop, it is not possible to use the two cameras together, thus we present here results from the high-speed camera only.

A simplified schematic diagram of the 3RFL is given in Fig. 4. It illustrates the position of 3RFL elements at horizontal (left panel, $\theta = 0$) and tilted (right panel, $\theta = 45°$) positions. One may notice that the rocking angle θ corresponds to the angle between the platform and the x-y plane. The rocking angle of the platform is governed by the position of the central shaft (F in Fig. 4) along the z-axis. This is possible as (i) the platform and the central shaft are connected by a universal joint (Fig. 5), (ii) the rotor (B in Fig. 4) and the slave rotor (D in Fig. 4) are linked by the connecting rod (C in Fig. 4).The universal joint is given in Fig. 5, and consists of two yokes attached by the cross-piece. The top yoke (red) is attached to the slave rotor,

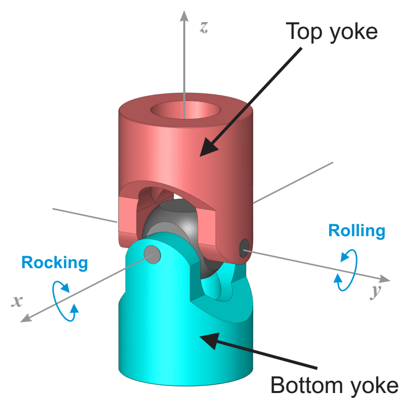

Figure 5: An illustration of the universal joint used in the 3RFL consisting of the top and bottom yokes and a cross-piece in between. The top yoke performs rockings along the x-axis and rollings along the y-axis, while the bottom yoke is motionless

while the bottom yoke (blue) is attached to the top end of the central shaft. The bottom yoke is motionless, whereas the top yoke manoeuvres easily in the x and y axes (the rotation around the z-axis is prevented). Notably, the top yoke rocks along the x-axis and rolls along the y-axis. Given that the slave rotor and the platform are linked, the inclination of the platform is due to the connecting rod (C in Fig. 4), which compensates for the displacement of the shaft by pulling the slave rotor (B in Fig. 4) down. As a result, the position of the connecting rod determines the location of the lowermost part of the platform and of the ring loop. In practice, the platform tilting is powered by the electrical motor shown in Fig. 4. The electrical motor (3-phase AC asynchronous motor, HPC Europe) induces the rotation of the drive shaft (A in Figs. 2, 4). Then, the rotation of the drive shaft is transmitted to the rotor (B in Fig. 4) by means of gears. The connecting rod is attached to the rotor by one end and loosely attached to the slave rotor by another end. As a result, the connecting rod rotates with the rotor while pulling down the sequential parts of the periphery of the slave rotor. Thus, the rotational motion of the drive shaft is transformed into rocking and rolling of the platform.

In this regard, Fig. 6 displays the interplay between the rotation of the rotor and the position of the ring loop. For clarity, the reference frames of the bottom and top yokes are defined as (x,y,z) and (x',y', z'), respectively, and the axis length is taken equal to the ring loop radius. When the drive

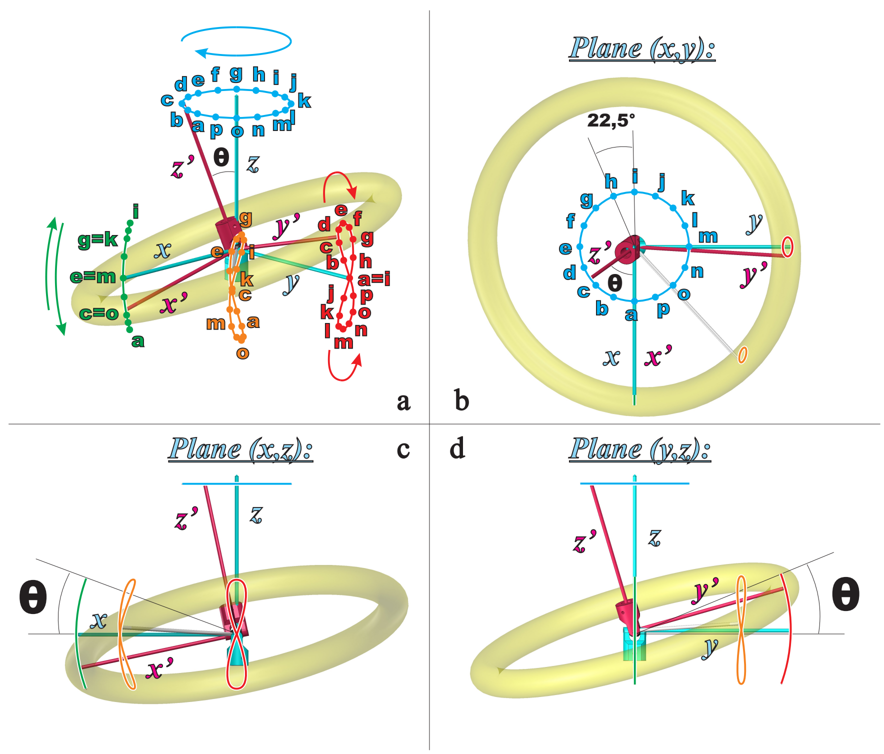

Figure 6: The sketch shows the positions of the ring loop corresponding to the positions of the upper yoke while performing a single tour about the z-axis at an inclination angle θ. Different views are shown: (a) general, (b) in the plane (xy), (c) in the plane (xz) and (d) in the plane (yz).

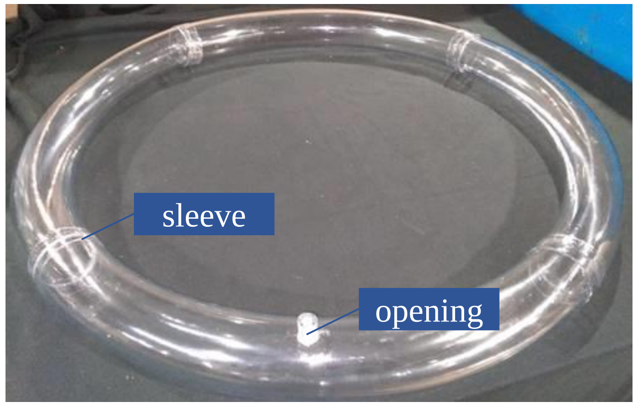

Figure 7: Cellulose acetyl butyrate tube with a diameter of $d = 69.85$ mm with one opening for fluid loading. Sleeves are made to strengthen tube connections.

shaft (A in Fig. 4) rotates, the central axis (Oz') of the top yoke draws a cone of half-angle θ around the bottom yoke central axis (Oz). The top yoke and the platform share the same central axis (Oz'). Also, the axial line of the ring loop is aligned with the center of the universal joint ball. To illustrate via Fig. 6 the interplay between the positions of the yoke and of the ring flow loop, 16 points (marked in blue as $a - p$) are picked up along the trajectory followed by the z'-axis corresponding to a complete revolution (360°) of the rotor (the baseline of the cone in blue). The corresponding trajectories of the $x'-$ and y'-axis are marked by green and red lines, respectively. The x' tip draws an arc, which yields the rocking motion. Meanwhile, the y' tip draws an eight-shape trajectory whose centre coincides with the tip of the $y-$axis. The eight-shape movement results in the rolling motion. In this way, the successive variations of the ring loop position cause fluids to circulate along the tube.

The employed ring loop, shown in Fig. 7, is made of cellulose acetyl butyrate (CAB) and has one opening for injecting and draining the test fluids. The optical clarity of the CAB tube allows an easy flow observation in any part of the system, while its physical strength ensures the stability of the loop throughout the experiments. The CAB ring loop comprises four 90° bend tubes solvent welded together. The tube connections are additionally strengthened by CAB sleeves (Fig. 7). The resulting ring loop dimensions are provided in Table 2.

2.2. Experimental procedure

The flow experiments aim to characterize air-water flow regimes and identify the emergence of specific flow patterns based on system control parameters. The 3RFL depicted in Fig. 2 is employed to conduct flow experiments at ambient temperature and atmospheric pressure. Flow regimes are determined based on direct observation of flow structure within a transparent tube. Certainly, a more advanced experimental methodology might be developed, and superior experimental methods (confocal laser sensor, capacitance probe, ...) might be introduced in the 3RFL apparatus. However, we would like to stress here that the aim of our work is to build a novel and compact experimental apparatus to mimic multiphase flows for petroleum engineering, *e.g.* under pressure, multiphase and reactive environment (formation of gas hydrates at the water-gas-oil interface). Clearly, the employment of alternative and more advanced experimental methods should be carefully handled given the harsh experimental conditions ($P > 80$ bar and $T < 4°$) we aim at reproducing in future. Indeed such an analysis is under consideration for future studies.

To enhance flow visualization, blue methylene powder ($\rho = 1310\ kg/m^3$; Sigma-Aldrich) is added to water ($\rho = 998.23\ kg/m^3$, $\mu = 1.002\ mPa\,s$) in a proportion of 1 mg per 1 litre. Coloured water is then loaded into the 3RFL through the opening with the aid of a syringe, while the residual air ($\rho = 1.2\ kg/m^3$, $\mu = 0.01813 mPa\,s$) in the ring loop is considered the gas phase. Table 2 lists the range of variation of control parameters employed in the experimental campaign.

The flow experiment is initiated by manually adjusting the rocking angle using a turning nut and hand wheel (H and I in Fig. 2). The rocking rate is controlled by adjusting the power input of the electric motor, which is then turned on. To analyze the impact of each particular control parameter on air-water flow regimes, the one-factor-at-a-time approach is employed. This approach consists in modifying one control parameter while keeping two others fixed and repeating the process for each of the control parameters.

Flow regime observations are carried out when the flow becomes fully developed. Our experiments showed that flow regime becomes fully developed after $2 - 4$ full revolutions of the liquid around the ring loop, which corresponds to $6 - 30$ seconds based on the rocking rate. We take advantage of the flow loop transparency and the high-speed camera to record the experiments on video and verify flow observations. The observed flow regimes are categorized and plotted on a flow regime map.

Control Parameters	Notation	Unit	Range
Rocking rate	f_R	opm	5.81-33.34
Rocking angle	θ	°	1-15
Diameter of the ring	D	mm	840
Diameter of the tube	d	mm	69.85
Liquid volume fraction	φ_L	-	0.03-0.15

Table 2: Range of control parameters used during the experiments.

To analyse average liquid height and average air bubble diameter, flow videos are converted into image sequences using the ImageJ software. As shown in the top left panel of Fig. 8, from 4 to 7 sub-images are selected from each image sequence to reproduce the lateral view of the liquid over subsequent regions. Liquid height and bubble diameter measurements are carried out using a ruler tool. As the only known distance is the tube diameter, this is used as the system's calibrating parameter. In addition, repeated measurements (228 measurements) of the diameter d_{cam} across flow images were taken to account for optical distortions caused by the tube's curvature and rocking motion.

As shown in the top-right panel of Fig. 8, to analyse the local liquid height, the distance between the gas-liquid interface and the bottom of the tube is measured and denoted as h_{cam}. From each image, at least 10 measurements were taken for a total of 40-90 measurements per flow case. For flow pattern displaying air bubbles, those are manually detected and sized (d_b) as shown in the bottom panel of Fig. 8. Experimental uncertainty measurements is described in section 2.3.

According to experimental investigations on two-phase flow in coiled tubes in the literature, we expect that the curvature-induced centrifugal force will drive the heavier phase, *i.e.* the liquid phase, towards the outer wall (O), as depicted in the top right panel of Fig. 8. As the flow images for liquid height measurements are taken from the outer wall, there is a possibility of a measurement discrepancy, as the local liquid height value (h_L), red line) could be smaller than h_{cam}. Therefore, it is crucial to establish the relationship between h_{cam} and h_L accounting for the potential impact of tube

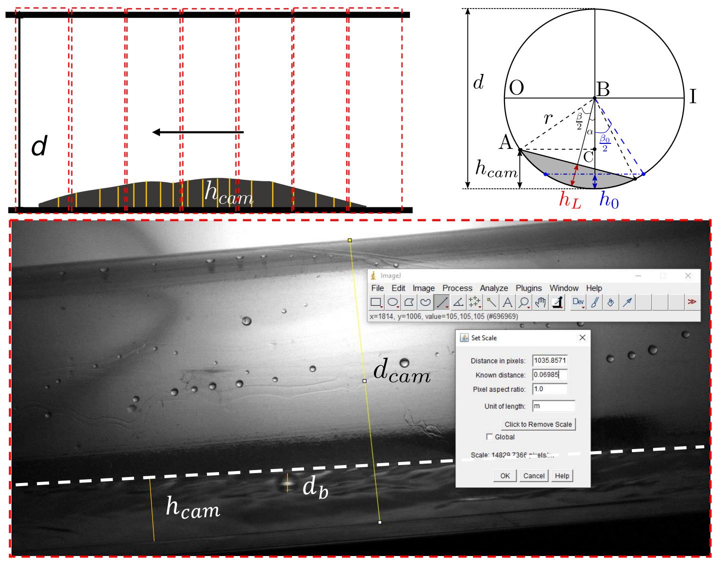

Figure 8: A sketch of the liquid height (h_L) and bubble diameter (d_b) measurement procedure. The red rectangles (top left panel) correspond to one image in the sequence. The bottom panel presents a random flow image in the software interface where d_{cam} is the tube diameter and h_{cam} is the local liquid height.

curvature.

For this, we introduce the hydraulic angle β (Fig. 8), which corresponds to an angle whose vertex is at the centre of the tube cross section and whose arms are radii intersecting two distinct points, where the liquid film touches the tube perimeter. In radians, the value of the hydraulic angle is ranged between 0 (gas-filled pipe) and 2π (liquid-filled pipe). From geometrical considerations of the circular segment, the liquid height h_L can be expressed using the hydraulic angle and radius of the tube r:

$$h_L = r(1 - \cos\frac{\beta}{2}) \tag{1}$$

To evaluate $\beta/2$, in Fig. 8 we represent a triangle ABC, where AB is equal to the radius of the tube, AC connects the wall-liquid contact point A with the vertical centre line of the tube segment by an angle $\pi/2$, and $BC = r - h_{\text{cam}}$. Therefore, Eq. 1 can be rewritten as:

$$h_L = r(1 - \cos(\pi/2 - \arcsin\frac{r - h_{\text{cam}}}{r} - \alpha)) \tag{2}$$

where α denotes the deviation between the vertical radius and h_{L_i}. Following Zhu et al. (2019), α can be recovered from the relation between centrifugal and gravitational forces and reads:

$$\alpha = \arctan\left(\frac{2U_L^2 \cos\theta}{gD}\right) \tag{3}$$

where θ is the rocking angle, g is gravitational acceleration, D is the diameter of the ring loop and U_L is the average liquid velocity. U_L can be defined as a function of the rocking rate (f_R) of the system and the radius of the ring loop (R):

$$U_L = \frac{2\pi f_R R}{60} \tag{4}$$

This relation is justified by our experiment, where it is found that the periods of rotation of the liquid phase and of the central shaft are the same despite the variation in rocking angle and liquid volume fraction. Such that, the tilt angle (Eq. 3) is a function of the control parameters of the system.

In this way, local liquid height h_L is calculated by employing system control parameters and high-speed camera measurements (h_{cam}). One must note that: *(i)* the procedure given in Eq. 2 applies to the case where the air-water interface is tilted from the horizontal. Otherwise, *i.e.* when the air-water interface is parallel to the horizontal plane and symmetrical with respect to the vertical centre line of the tube segment, $h_{\mathrm{cam}} = h_L$. *(ii)* Eq. 2 is valid only for a flat gas-liquid interface in the cross-sectional area. It will be shown later (Table 4) that in our 3RFL set-up, the air-water interface in radial direction is not always flat for all observed flow patterns. However, although the interface is slightly curved in the cross section, the deviation from the flat configuration is not very high due to the small rocking angles adopted here. For instance, when the rocking angle is set to 0°, regardless of the rocking rate, the loop does not have any motion and thus the fluid is static. Finally, the average liquid height $\overline{h}_L$ and average bubble diameter $\overline{d}_b$ were calculated as an arithmetic mean of the corresponding local liquid height and air bubble diameter values:

$$\overline{h}_L = \frac{1}{n}\sum_{i=1}^{n} h_{L_i}\ , \qquad \overline{d}_b = \frac{1}{n}\sum_{i=1}^{n} d_{b_i} \tag{5}$$

where h_{L_i} and d_{b_i} are the single measurement.

2.3. Experimental uncertainties

This section presents uncertainty analysis conducted for the measurements of average liquid height ($\overline{h}_L$) and average bubble diameter ($\overline{d}_b$). In compliance with the International Organization for Standardization (ISO), assessment of uncertainty entails consideration of Type A and Type B uncertainties (2008ISO/IEC2008). Type A uncertainty arises from repeated observations, while Type B uncertainty is based on all available information about the measurand's variability, such as previous measurements, instrument specifications, calibration data, and reference data from handbooks.

Given that $\overline{h}_L$ is evaluated as the mean of n independent observations, Type A uncertainty is estimated as a relation of standard deviation of the mean to the square root of the number of observations (2008ISO/IEC2008):

$$\mathcal{U}(\overline{h}_L) = \frac{1}{\sqrt{n}} \frac{\sum_{i=1}^{n}(h_{L_i} - \overline{h}_L)}{\sqrt{n-1}} \ . \tag{6}$$

As noted in the experimental procedure, whether the liquid flow is tilted or not defines the relation between h_{L_i} and h_{cam_i}. It is notable that Type A uncertainty varies for each studied case since the tilt angle α and the number of observations n may change. In the present case, Type B uncertainty stems from the uncertainty of the tube diameter dimension used for system calibration and instrument uncertainties related to optical distortions (Fig. 8). We will now assess each of these two uncertainties and then we will integrate them into the combined uncertainty along with Type A uncertainty calculated based on Eq. 6.

We start by assessing the tube diameter uncertainty. The tube diameter was determined as the average value of 20 measurements conducted using a Vernier caliper. The uncertainties related to the diameter measurement are as follows: *(i) Type A* uncertainty, calculated as the standard uncertainty of the mean, i.e., the population standard deviation divided by the square root of the number of observations, yielding $\pm 0.003mm$ (2008ISO/IEC2008):

$$\mathcal{U}(\overline{d}) = \frac{1}{\sqrt{n}} \frac{\sum_{i=1}^{n}(d_i - \overline{d})}{\sqrt{n-1}} \ , \tag{7}$$

where $\overline{d} = 1/n \sum_i^n d_i$ is the mean value of the tube diameter measurements and n is the number of measurements; *(ii) Type B* uncertainty, assigned by instrument accuracy, which is half of the smallest increment of the Vernier caliper, *i.e.*, ±0.01 mm. The combined uncertainty of the tube diameter, $\mathcal{U}_c(\overline{d}) = \pm 0.01$ mm, is calculated as the root sum of the squares of Type A and Type B uncertainties. This total standard uncertainty is associated with a 68% confidence level. To expand the confidence interval to a 95% level, a coverage factor of 2 is applied, which is obtained from Student's t-distribution. Finally, the expanded uncertainty of the tube diameter is $U(\overline{d}) = \pm 0.02$ mm, corresponding to a 95% confidence level.

Uncertainties related to optical distortions from tube curvature, position variations, and instrument precision were addressed by analyzing 138 images at a rocking angle of $\theta = 5°$. These images represent all possible variations in the position of the observed tube segment corresponding to a complete revolution of the liquid around the loop. This yielded 228 outer diameter measurements (d_{cam_i}):

1. 138 values correspond to punctual measurements of the outer diameter (at the center of the image) to address variations in segment position due to rocking, as the tube is moving up and down (see for instance Fig. 10).
2. 20 values are obtained by moving from left to right within one image with small increments, aiming to account for optical distortions at the image edges due to curvature.
3. 70 values are taken from 14 images (each tenth image), with five equally spaced measurements from each image to complete the sample.

Finally, the standard uncertainty of the mean $\overline{d}_{\text{cam}}$ (optical distortion uncertainty) is:

$$\mathcal{U}(\overline{d}_{\text{cam}}) = \frac{1}{\sqrt{n}} \frac{\sum_{i=1}^{n}(\overline{d}_{\text{cam}_i} - \overline{d}_{\text{cam}})}{\sqrt{n-1}} = \pm 0.02 \tag{8}$$

where $n = 228$. In contrast to Type A uncertainty, Type B uncertainties of average liquid height measurement will remain independent of flow conditions and will be the same for air bubbles diameter measurements.

Finally, the combined uncertainty of the average liquid height $\mathcal{U}_c(\overline{h}_L)$ is then calculated as square root of sum of squares of Type A and Type B uncertainties:

$$\mathcal{U}_c(\overline{h}_L) = \sqrt{\mathcal{U}(h_L)^2 + \mathcal{U}_c(\overline{d})^2 + \mathcal{U}(\overline{d}_{\text{cam}})^2} \tag{9}$$

This combined standard uncertainty is associated with a 68% confidence level. To achieve a 95% confidence level, the resulted $\mathcal{U}_c$ value is multiplied by 2.

The uncertainty of average bubble size measurement comprises Type A uncertainty stemming from repeated measurements and Type B uncertainty, i.e. instrumental uncertainty. Type A uncertainty of the mean is obtained by dividing the standard deviation of the bubble diameter measurements by the square root of the number of observations. As number of detected air bubbles varied wrt. the rocking rate, Type A uncertainty varied. Meanwhile, Type B uncertainty remains unchanged with respect to that of liquid height measurements. Finally, the combined uncertainty is estimated as the root of the sum of squares of Type A and Type B uncertainties, then multiplied by a coverage factor equal to 2 to yield an expanded uncertainty, *i.e.* corresponding to 95% confidence level.

2.4. Dimensionless parameters of the flow

Air-water flow regimes result from the balance of various forces acting on the system and are also affected by pipe geometry and fluid characteristics. We consider gravity, viscous, inertial, surface tension, and centrifugal forces as significant factors in our system. To understand the nature of flow regime transition (see Section 3), we evaluate the dimensionless numbers Reynolds, Weber and Froude based on (Murai et al., 2006). The ratio of inertial to viscous forces is determined by the Reynolds number:

$$Re = \frac{\rho_L h_0 U_L}{\mu} \tag{10}$$

where ρ and μ are the density and the dynamic viscosity of the fluid and U_L is the average velocity of the liquid phase. From Fig. 8, h_0 is a reference liquid height, corresponding to the thickness of the liquid film at the centre of the cross-sectional area when the system is static and the ring is horizontal. In other words, it is the maximum film thickness in the section at rest: $h_0 = \max[h(f_R = 0, \theta = 0)] = h_L(f_R = 0, \theta = 0)$. Note that h_0 and h_L are not equal as the liquid might experience de-wetting in the axial direction. The reason why h_0 is chosen as reference scale (rather than the pipe diameter) is mainly due to our two-phase flow, which is not driven by pressure gradient. In this condition, the gas is solely driven by the shear exerted by the liquid. From the geometry of the pipe segment, h_0 may be expressed as:

$$h_0 = r(1 - \cos\frac{\beta_0}{2}) \tag{11}$$

where r is the radius of the tube and β_0 is the hydraulic angle when both the rocking rate and the rocking angle are set to zero, in other words β_0 is

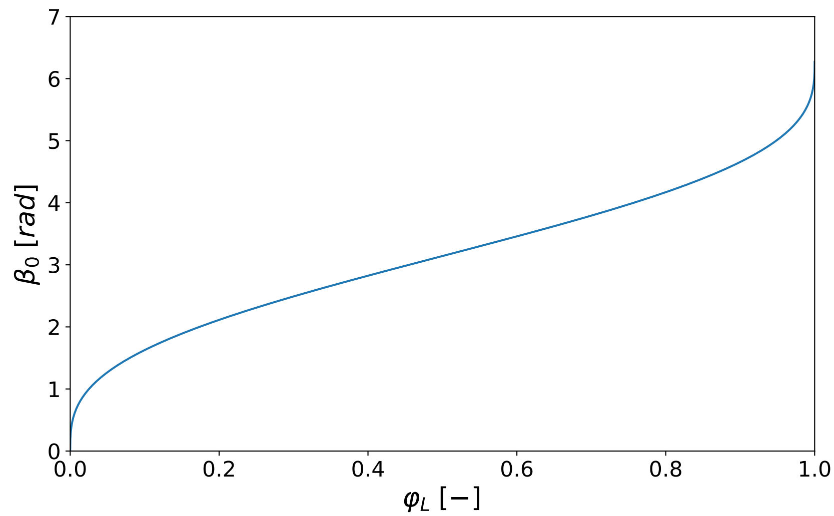

Figure 9: Hydraulic angle at the state of rest of the air-water flow as a function of liquid volume fraction (Eq.14).

the angle subtended by the liquid phase in the pipe segment at rest (Fig. 8). The value of β_0 depends on the volume of the liquid phase, *i.e.* the liquid volume fraction φ_L. The latter can be expressed as a relation of the area of the liquid phase in the cross-section of the pipe (A_L) to the total area of the pipe segment (A_P):

$$\varphi_L = \frac{A_L}{A_P} \tag{12}$$

Following Lee et al. (2013), the geometrical parameters in the tube segment can be expressed in terms of r and β:

$$A_P = \pi r^2 \qquad A_L = \frac{1}{2} r^2 (\beta - \sin\beta) \qquad A_G = A_P - A_L \tag{13}$$

Upon substitution one obtains:

$$\varphi_L = \frac{\beta_0 - \sin\beta_0}{2\pi} \tag{14}$$

The solution of Eq. 14 is showed in Fig. 9, which allows to estimate h_0. Low Re numbers lead to laminar flow, where viscous forces are not negligible as in a turbulent flow. Indeed, the laminar flow is mainly characterized by a

Non-dimensional number	Values
Fr	0.25 − 5.47
Re	1287 −22153
We	5 − 463

Table 3: Range of values of the non-dimensional numbers considered in this study.

parallel flow. The relationship between surface tension and inertial forces is expressed by the Weber number:

$$We = \frac{\rho U_L^2 h_0}{\sigma} \tag{15}$$

At low We numbers, the surface tension forces which tend to stabilize the flow, prevail. The Froude number corresponds to the relation between centrifugal and gravitational acceleration:

$$Fr = \sqrt{\frac{\omega^2 \, R}{g \sin \theta}} \tag{16}$$

where g is the gravitational acceleration, θ is the rocking angle, R is the radius of the ring and ω is angular velocity. We have also verified that centripetal forces U_L^2/R are much smaller than gravitational forces and do not affect the value of g significantly. When the Fr number is high, centrifugal forces dominate the flow. Table 3 summarizes the Fr, Re and We values calculated for the studied system. An analysis of such values, $Re > 1$ and $We > 1$, indicates that inertial forces dominate over viscous and surface tension forces. Meanwhile, Fr values ranging from 0.25 to 5.47 indicate that depending on the flow conditions, gravitational or centrifugal forces may prevail.

3. Experimental results

3.1. Observed air-water flow regimes

Varying system control parameters such as the rocking angle θ, rocking rate f_R, and liquid volume fraction φ_L resulted in different air-water flow regimes. Based on visual observations, three flow regimes are identified such as smooth interrupted, wavy-bubbly continuous and smooth continuous. Table 4 provides illustrations of the observed flow regimes as seen from both

Flow Regime	**Stream-wise sketch**	**Radial sketch**
Smooth Interrupted (**SI**)	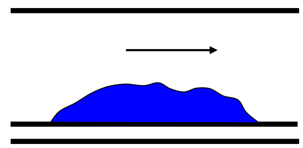	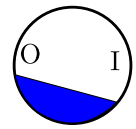
Wavy-Bubbly Continuous (**WBC**)	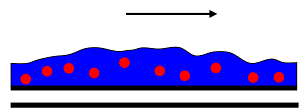	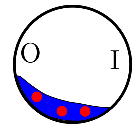
Smooth Continuous (**SC**)	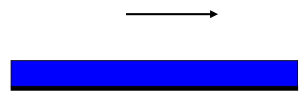	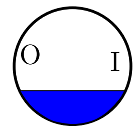

Table 4: Air-water flow regimes observed in the 3RFL.

a stream-wise and radial perspective. Flow images of corresponding flow regimes are given in Fig. 10. For better comprehension, you may refer to the videos of flow regimes in the supplementary materials.

The Smooth Interrupted (SI) regime defines the configuration for which the liquid flows at the bottom of the tube in the form of a hump (A in Fig. 10) while the rest of the tube is dewetted. Notably, this hump flows following the lowermost part of the ring loop during successive rockings and rolling, meaning that the downward gravity is a driving force of the flow. The gas-liquid interface is mainly smooth or has ripples. Depending on the rocking rate flow can be symmetrical and asymmetrical with respect to the vertical centre line of the tube cross section.

The Wavy-Bubbly Continuous (WBC) regime identifies the flow configuration for which the bottom of the tube is fully wetted in its length and the gas-liquid interface is wavy-bubbly (B in Fig. 10). Meanwhile, as shown in Table 4, during WBC, the gas-liquid interface is asymmetrical with respect to the vertical diameter of the tube cross-section. Indeed, the level of liquid at the outer wall is higher than at the inner wall. Following Murai et al. (2006); Banerjee et al. (1969) this can be explained by the effect of curvature-induced centrifugal force which pushed the dense phase, *i.e.* liquid phase, towards the outer wall. Flow images of wavy-bubbly continuous flow allowed us to characterize air bubble behaviour throughout the flow. It is observed that air bubbles have a spherical shape. We suggest that bubbles

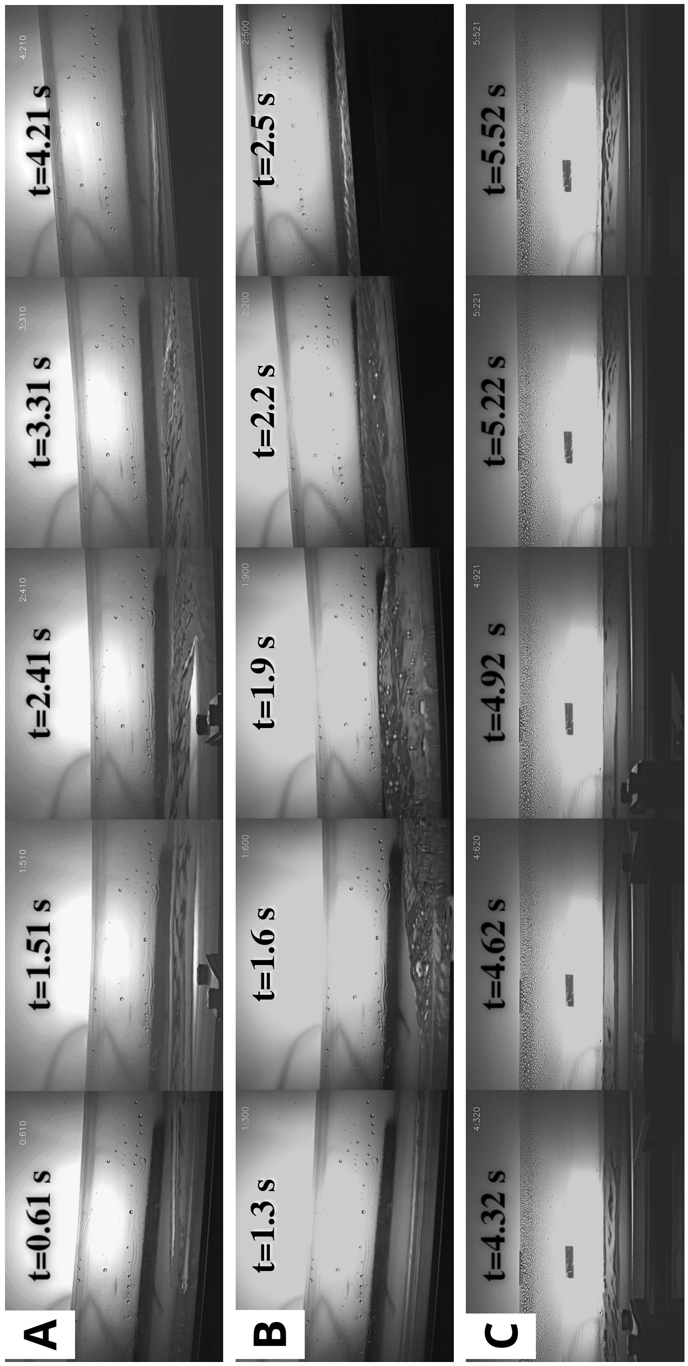

Figure 10: Air-water flow regimes: (A) smooth interrupted, (B) wavy-bubbly continuous and (C) smooth continuous.

entrap into the liquid phase due to the curvature-induced secondary flow. The secondary flow is characterized by the migration of the fluid from the inner side of the tube toward the outer wall by tube walls and returning to the inner wall by the horizontal central line (Dean, 1927). This initiates radial mixing, causing some parts of the liquid phase to collide with each other in the presence of air, resulting in the entrainment of air within the liquid. Besides, the radial mixing promotes air bubble collisions, which leads to their flocculation and coalescence. This observation is consistent with Kaji et al. (1984) and Murai et al. (2006). From our observations, bubbles are able to grow into agglomerated structures that subsequently dissociate (see video 5 in supplementary materials). The analysis of air bubble size and distribution will be conducted in Section 3.4.

The Smooth Continuous (SC) regime corresponds to the flow structure for which the liquid is uniformly distributed over the entire length of the ring. Here the elevation of the liquid is the same all along the pipe, despite the successive tilting of the ring loop (C in Fig. 10). In some way, such flow behaviour recalls the wall-clinging effect described by Murai et al. (2006) for which the liquid bulk is forced to reside at the bottom of the tube due to the strong influence of centrifugal forces on the system. Meanwhile, the gas-liquid interface is smooth or may have ripples. Also, the flow is symmetrical in the radial cross-sectional area. Now we analyse the impact of system control parameters on flow regime occurrence.

3.2. Effect of system control parameters on flow regimes

In Fig. 11, the flow regime maps for the observed air-water flow regimes in the 3RFL with a diameter of $d = 69.85$ mm are shown. The liquid volume fraction (φ_L) is represented on the x-axis, while the rocking angle (θ) is represented on the y-axis. The ten panels correspond to different values of the rocking rate f_R. The flow regime boundaries are indicated by a black dashed line. The blue triangles, red circles, and grey squares in the figure indicate the smooth interrupted (SI), wavy-bubbly continuous (WBC), and smooth continuous (SC) regimes, respectively. The green stars correspond to flow regimes difficult to identify as either SI or WBC.

At small rocking rates ($f_R \leq 8.51$ opm, panels in the first line), mainly the SI regime occurs for all θ and φ_L. As the rocking rate increases ($9 < f_R < 14$ opm, panels in the second line), the WBC regime starts to occur at low θ for each considered φ_L. By further increasing f_R ($f_R = 16.78$ opm, fifth panel), the SC regime occurs now at low θ for each φ_L, whereas the

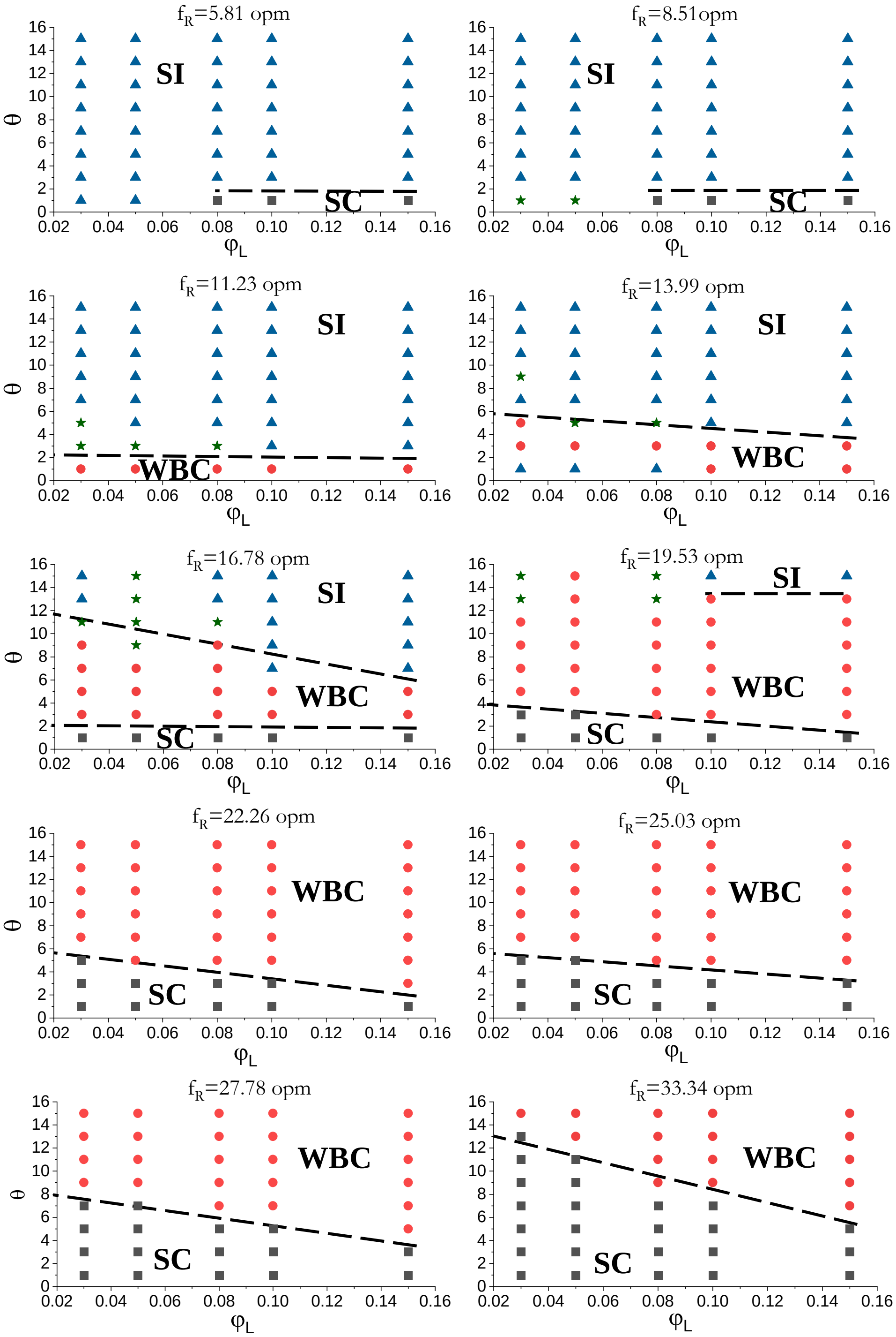

Figure 11: Air-water flow regime map.

WBC regime expands at larger θ, leading to the SI regime to disappear ($f_R = 22.26$ opm, seventh panel). At even larger values of f_R ($f_R > 23$ opm, eighth to tenth panel), the SC regime occurs at larger θ and widens.

Flow regime transition boundaries are also governed by inclination angle and volume fraction. As the liquid volume fraction increases, SI-WBC and WBC-SC transitions take place at smaller rocking angles. The combination of low rocking angles, high rocking rates, and high liquid volume fraction leads to an increased effect of the gravity force, promoting a smooth interrupted flow. As the rocking rate rises, the influence of centrifugal forces on the flow becomes more pronounced. This causes some liquid to accumulate at the bottom of the tube, transitioning the flow from an interrupted regime to a continuous one, such as smooth continuous (SC) or wavy-bubbly continuous (WBC) flow. In particular, the WBC flow regime arises when liquid loading, rocking rate, and angle are large, whereas when the rocking rates are high, and the rocking angles are low (θ=1-5°), centrifugal forces overcome gravity, leading to the occurrence of the SC regime. In what follows, flow regime transitions will be analysed using previously defined dimensionless parameters of the flow.

Figure 12 collects all the experimental data obtained by varying the control parameters as in Table 2. In particular, Figure 12 shows the flow regime maps in the Fr-We plane (top panel) and in the Fr-Re plane (bottom panel). Again, blue triangles indicate smooth interrupted (SI), red circles indicate wavy-bubbly continuous (WBC) and grey rectangles indicate smooth continuous (SC) regimes. Flow regimes which are questionable to identify as SI or WBC are marked by green stars. Flow regime boundaries are shown by black dashed lines. Flow regime transition boundaries have a steep slope, which indicates that they are highly dependent on the value of the Fr number. This suggests that the relation between centrifugal and gravitational forces plays a crucial role in the appearance of a particular flow regime. Indeed, when the flow is mainly governed by the gravity force, *i.e.* when $Fr < 1$, the smooth interrupted flow is promoted (blue triangles). As the centrifugal force is dominant over gravity ($Fr > 2$), the flow is smooth continuous (grey rectangles). This can be attributed to the centrifugal force-promoted wall-clinging effect reported in literature (Murai et al., 2006; Akagawa et al., 1971). Now, the total liquid volume is evenly distributed throughout the loop.

In the intermediate region where $1 < Fr < 2$, there exists a competition between gravity and centrifugal forces, leading to an intermediate and

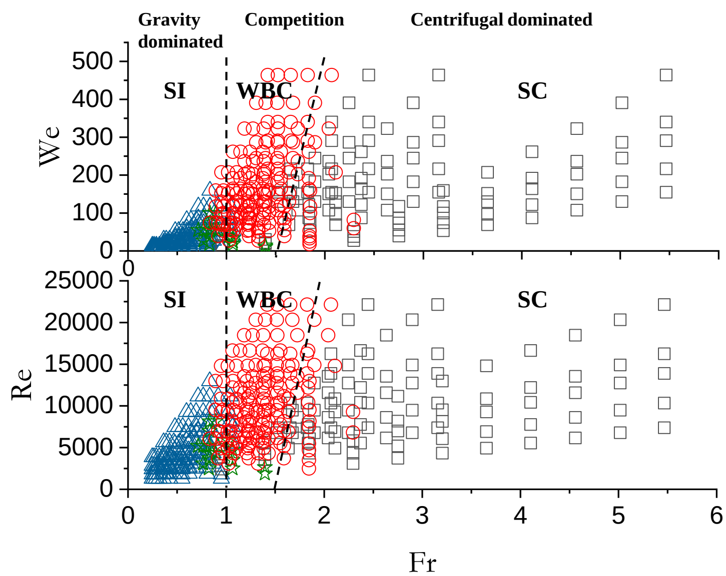

Figure 12: Flow regime map $(Fr - We)$ (top) and $(Fr - Re)$ (bottom) of air-water two-phase flow in the 3RFL with $d = 69.85$ mm. SI regime - blue triangles, WBC regime - red circles, SC regime - grey rectangles and there are controversial cases marked by green stars, where the regimes are either SI or WBC.

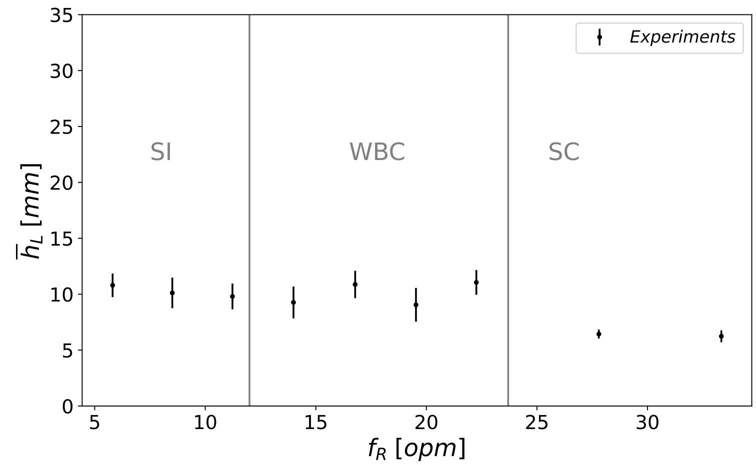

Figure 13: Results of the liquid height measurements for the air-water flow in 3RFL with d=69.85 mm, $\varphi_L = 0.05$, $\theta = 5^0$ and different rocking rates.

disturbed wavy-bubbly continuous (red circles) flow.

3.3. Liquid height measurements

To compare the experimental results to the different modelling strategies (section 4.4), we present here the experimentally obtained liquid heights. In Fig. 13 results for the average liquid height h_L are shown (black dots) as a function of rocking rate, by accounting for the measurement error, through error bars, as described earlier. The chosen configuration consists of $\varphi_L = 0.05$ and $\theta = 5°$. Grey vertical lines refer to the flow regime boundaries, as observed experimentally. By comparing the liquid height values for SI and SC regimes, one may notice that the layer of the liquid thins for the latter. Meanwhile, for the WBC regime, the average height of the liquid is almost the same as the SI regime or slightly increases with the rocking rate f_R. The reason for this increase is twofold. First, the presence of air bubbles entrapped inside the liquid layer finally raises the level of the liquid. Secondly, the centrifugal force pushes the liquid towards the outer wall causing the asymmetry of the level of the interface. Therefore, the height of the liquid level on the outer side is higher than on the inner side (see Table 4). Given that analysed images are taken from the outer wall explains the discrepancy.

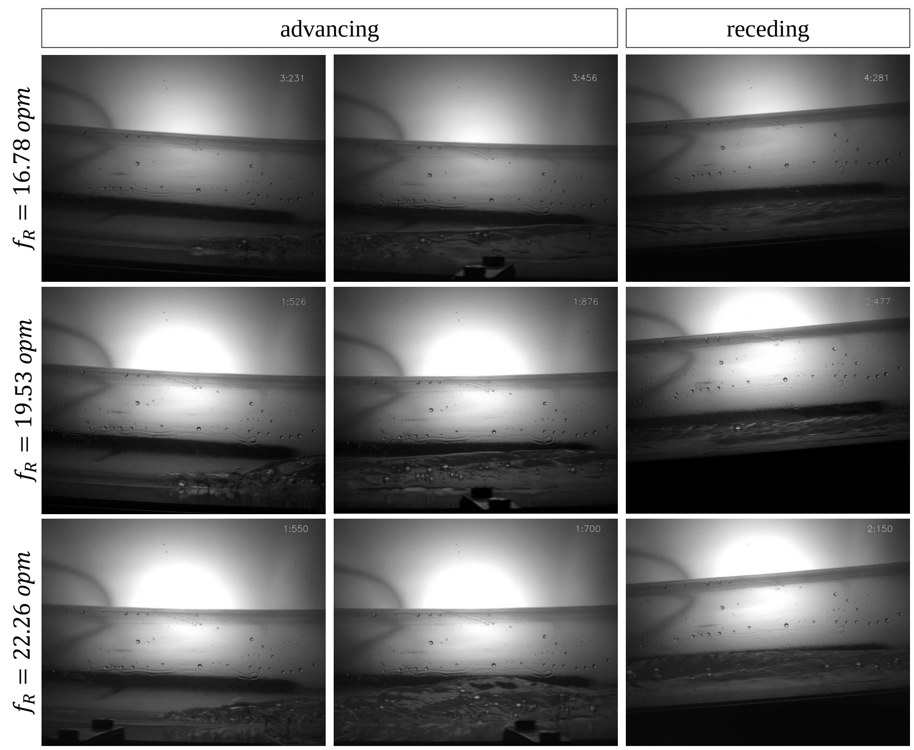

Figure 14: Images of advancing and receding parts of the air-water bubbly flow at various rocking rates: $f_R = 16.78$ opm (1st row), 19.53 opm (2nd row), and 22.26 opm (3rd row).

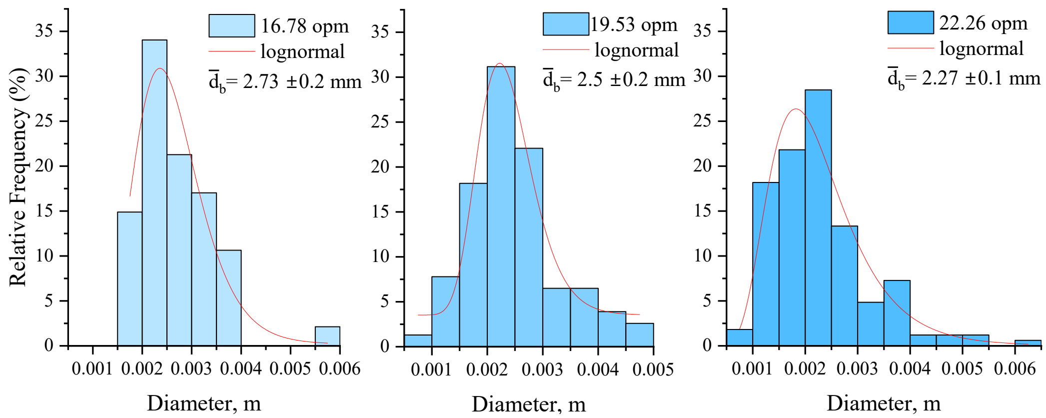

Figure 15: Results on the relative frequency of bubble size estimated for the air-water bubbly flow in 3RFL with d = 69.85 mm with φ_L = 0.05, $\theta = 5^0$ and f_R = 16.78 opm (left panel), 19.53 opm (central panel) and 22.26 opm (right panel). A curve in red is a log-normal curve.

3.4. Air bubbles size and distribution

Fig. 14 demonstrates flow images of different parts of the wavy-bubbly continuous flow, *e.g.* the advancing and receding parts, at θ=5$\circ$, $\varphi_L = 0.05$ and various rocking rates including f_R = 16.78 opm, 19.53 opm, and 22.26 opm. It is noticed that the air bubbles in the WBC flow are non-homogeneous in terms of size and distribution. In regard the distribution, it is observed that the main volume of bubbles is concentrated in the advancing part of the flow, while the receding part of the flow contains few or no bubbles. Besides, in Fig. 14, one may note that an increase in the rocking rate produces more bubbles meaning that the secondary flow becomes more pronounced.

Now, we focus on the results of the bubble size analysis obtained by image processing. Fig. 15 displays the relative frequency of bubble size distribution at various rocking rates. As one may note, the bubble size distribution fits into the log-normal curve (red line, Fig. 15). With an increase in the rocking rate, the number of detected bubbles increased from 47 (for f_R = 16.78 opm) to 165 (f_R = 19.53 opm), which justifies our observations. However, it is found that the mean diameter $\overline{d}_b$ decreases with the rocking rate. This shows that the more bubbles are entrapped, the more they are fractured.

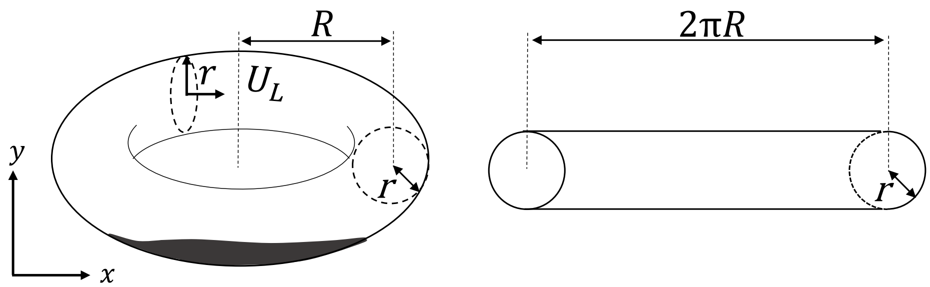

Figure 16: Sketch of the horizontal ring loop, where r is the radius of the tube and R is the radius of the ring, and U_L is the average velocity of the liquid phase.

4. Air-water flow modelling and validation

As shown in Fig. 13, the experimental analysis provides the average liquid heights in the 3RFL for all studied flow regimes. We now complement the experimental analysis with modeling development, which might be helpful to study the effect of varying fluid properties and flow conditions, *e.g.* replacing water with oil. Therefore, in this section we focus on the development of a modelling strategy for the investigation of the air-water flow within the 3RFL. Three modelling approaches are applied to predict the average height of the liquid level h_L for the studied flow: mechanistic model, total energy minimization model and a combined approach. To begin with, we approximate the ring loop as a horizontal pipe as illustrated in Fig. 16. With this in mind, as shown in Fig. 17, we consider a downward inclined tube in which gas-liquid flow is driven by gravity and by an external force related to the rotation of the shaft. The liquid phase flows at the bottom of the conduit as heavier fluid. Also, we presume that the flow is incompressible and steady-state.

Before pursuing with the model development, it is noteworthy to mention that the final goal is to obtain modelled average liquid heights to compare to those obtained experimentally. Note that liquid heights h_L and hydraulic angles β are linked in an unique way (see Fig. 8 and Eq. 1). For this, for each of the three adopted modeling strategy, we have developed an equation solely enslaved to the hydraulic angle β. While expressing the areas occupied by the liquid and the gas, as well as the average liquid and gas velocities as a function of β is straightforward - as it will be shown later - this is not the case for the wall shear stresses, unless computed via empirical relations.

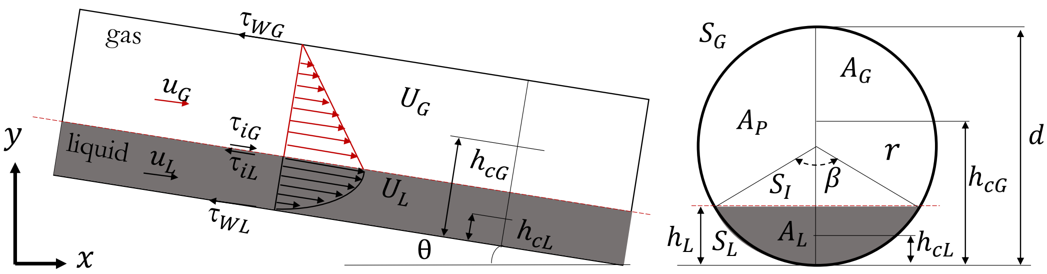

Figure 17: Sketch of the gas and liquid flow and velocity profiles in an inclined channel. Subscripts G, L and I denote gas, liquid and interface, d is the diameter of the tube, θ is pipe inclination angle, A is the area, S is the contact perimeter, h is height, U is average velocity, and u is velocity profile.

Therefore, closure relations are needed to express viscous terms as a function of β only. One way to accomplish this consists in deriving the liquid and gas velocity profiles, and then derive those to find the wall shear stresses. By assuming that the gas-liquid interface remains flat, the liquid velocity u_L is uniform in the stream-wise direction, thus $u_L = u_L(y)$. Also, the velocity profile is parabolic given the equilibrium between volumetric and viscous forces (Nusselt, 1916). Furthermore, since there is no applied pressure gradient, we suppose that the gas flows along the tube only due to the entrainment of the liquid layer. As a result, the gas velocity profile u_G is linear with the coordinate y, and in a similar way as the liquid, the gas velocity is uniform in the stream-wise direction, hence $u_G = u_G(y)$. Assuming no-slip velocity at tube walls, continuity of velocities and shear stresses at the gas-liquid interface as boundary conditions, one can obtain gas and liquid velocity profiles:

$$u_G = \frac{6U_L(d-y)}{h_L(\mu_G/\mu_L + 4d/h_L - 4)} \tag{17}$$

and

$$u_L = \frac{6U_L}{h_L^2}\frac{(1 - d/h_L - \mu_G/\mu_L)}{(\mu_G/\mu_L + 4d/h_L - 4)}y^2 + \frac{6U_L}{h_L}\frac{(\mu_G/\mu_L + 2d/h_L - 2)}{(\mu_G/\mu_L + 4d/h_L - 4)}y \tag{18}$$

where the condition for the average velocity $U_L = 1/h \int_0^{h_L} u_L(y)$ has been also employed. In Eqs. (17) and (18), d is the diameter of the tube, μ_G and μ_L are gas and liquid viscosities, h_L is the height of the liquid level. Note that h_L is still unknown. By definition of the flow within a conduit, U_L can be determined as a relation of the volumetric liquid flow rate Q_L to the cross-sectional area occupied by the liquid phase A_L:

$$U_L = \frac{Q_L}{A_L} \tag{19}$$

where $Q_L = V_L/t$, being V_L is the liquid volume within the pipe. As for the time t, we verified that the period of circulation of the liquid phase is equal to the rotational period of the rotor $60/f_R$. Thus, average velocity U_L reads:

$$U_L = \frac{V_L f_R}{A_L 60} \tag{20}$$

Again, U_L depends on the area occupied by the liquid, which is unknown as it depends on h_L (Eq. 13 and 1).

We are also interested in determining the wall and interfacial shear stresses. These can be derived either through empirical correlations or by derivation of the velocity profiles Eqs. (17) and (18). The latter leads to:

$$\tau_{WL} = \mu_L \frac{du_L}{dy}\bigg|_{y=0} = \frac{6U_L}{h} \frac{\mu_L(\mu_G/\mu_L + 2d/h - 2)}{\mu_G/\mu_L + 4d/h - 4} \tag{21}$$

$$\tau_{WG} = \tau_{iG} = \mu_G \frac{\partial u_G}{\partial y}\bigg|_{y=h} = -\frac{6U_L}{h} \frac{\mu_G}{\mu_G/\mu_L + 4d/h - 4} \tag{22}$$

$$\tau_{iG} = \mu_G \frac{\partial u_G}{\partial y}\bigg|_{y=h} \tag{23}$$

It comes out that the interfacial and the gas shear stresses are uniform and constant, whilst the liquid shear stress is linear with the cross-stream coordinate. Noteworthy is that velocity profiles (Eqs. 17 - 18) and shear stresses (Eqs. 21- 22) are functions of the fluid properties, tube diameter, position of the interface h_L (Eq. 1) and average velocity of the liquid phase U_L (Eq. 20). Now, h_L and U_L are functions of the variable parameter β. Therefore, the problem has been restructured as solely the hydraulic angle β remains as the parameter and all other quantities can be enslaved to β. In what follows, the mechanistic and the total energy minimization model as well as a combined approach will be applied to the above-described problem to predict the gas-liquid flow arrangement in terms of h_L (or β).

4.1. Mechanistic model

Considering the flow configuration described in Fig. 17, and following Taitel and Dukler (1976b) assumptions, the momentum conservation equations for each phase are:

$$-A_G\left(\frac{dP}{dx}\right)_G - \tau_G S_G + \tau_I S_I + \rho_G g A_G \sin\theta = 0 \tag{24}$$

$$-A_L\left(\frac{dP}{dx}\right)_L - \tau_L S_L - \tau_I S_I + \rho_L g A_L \sin\theta = 0 \tag{25}$$

where $\left(\frac{dP}{dx}\right)_G$ and $\left(\frac{dP}{dx}\right)_L$ are pressure gradients in the gas and in the liquid phases, whereas τ_G, τ_L, and τ_I are gas-wall, liquid-wall and gas-liquid interfacial shear stresses. Finally, g is gravitational acceleration, ρ_G and ρ_L are densities of the gas and the liquid phases, whereas θ is the inclination angle of the tube from the horizontal. From the momentum conservation one yields:

$$-\left(\frac{dP}{dx}\right)_G = \tau_{WG}\frac{S_G}{A_G} - \tau_I\frac{S_I}{A_G} - \rho_G g \sin\theta \tag{26}$$

$$-\left(\frac{dP}{dx}\right)_L = \tau_{WL}\frac{S_L}{A_L} + \tau_I\frac{S_I}{A_L} - \rho_L g \sin\theta \tag{27}$$

Presuming equality of pressure gradients in both phases, one can obtain a combined momentum equation:

$$F = \tau_{WG}\frac{S_G}{A_G} - \tau_{WL}\frac{S_L}{A_L} - \tau_I S_I\left(\frac{1}{A_G} + \frac{1}{A_L}\right) + g\sin\theta(\rho_L - \rho_G) = 0 \tag{28}$$

The next step is to express the forces engaged in the combined momentum equation. For the wall and interfacial shear stress, closure laws are needed. By applying the classical empirical correlations (Taitel and Dukler, 1976b), it follows that:

$$\tau_{WG} = \frac{f_G \rho_G U_G^2}{2} \tag{29}$$

and

$$\tau_{WL} = \frac{f_L \rho_L U_L^2}{2} \tag{30}$$

The interfacial shear stress reads:

$$\tau_I = f_I\frac{\rho_G (U_L - U_G)^2}{2} \tag{31}$$

Friction factors f_G, f_L, f_I can be expressed via the Blasius relations (Blasius, 1913):

$$f_L = C_L(Re_L)^{-n} = C\left(\frac{d_L U_L \rho_L}{\mu_L}\right) \quad (32)$$

and

$$f_G = C_G(Re_G)^{-m} = C\left(\frac{d_G U_G \rho_G}{\mu_G}\right) \quad (33)$$

where $C_L = C_G = 16$ and $m = n = 1$ for laminar flow ($Re < 2000$), whereas $C_L = C_G = 0.046$ and $m = n = 0.2$ for turbulent flow ($Re > 2000$). Following Chakrabarti et al. (2005), the friction factor at the interface is taken equal to the friction factor of the faster-moving phase, *i.e.* $f_I = f_L$.

It follows that the combined momentum equation (Eq. 28) is a function of liquid velocity, tube diameter, fluids properties and the hydraulic angle β (via U_L, U_G and A_L, A_G). To assess the net of momentum of the system (Eq. 28), both ways to compute shear stresses, *i.e.* produced via empirical correlations (Eqs. 29 - 30), and determined analytically, (Eqs. 21 - 22), are applied. The solution of the fully developed steady-state flow satisfies the condition when the net of momentum is zero. Fig. 18 displays the variations in the net of momentum (Eq. 28) depending on the hydraulic angle, where τ^E (red dashed line) and τ^A (green dot-dashed line) refer to the empirical correlations and analytical expressions of shear stress used for computations. Filled rectangles identify the condition when F=0. Thereby, the hydraulic angle corresponding to $F = 0$ will be assigned as the solution of the system. The solution of the system can be expressed in terms of the liquid height employing Eq. 1 and will be analysed in section 4.4.

4.2. Total Energy Minimization

The main idea of the energy minimization concept suggests that any natural system stabilizes to its minimum total energy. Applied to the studied flow, one can suppose that any air-water flow will be arranged in such a way as to minimize the energy to be transported. In particular, the air-water flow arrangement can be expressed in terms of the height of the liquid phase in the tube cross-section, which is correlated to the hydraulic angle β (Eq. 1). Thus, our aim here is to express the total energy of the two-phase flow as a function of β, then define the hydraulic angle which results in the minimum total energy.

The total energy of the air-water flow E_T is composed of potential E_P, kinetic E_K and surface E_S energies. Considering the air-water flow with the

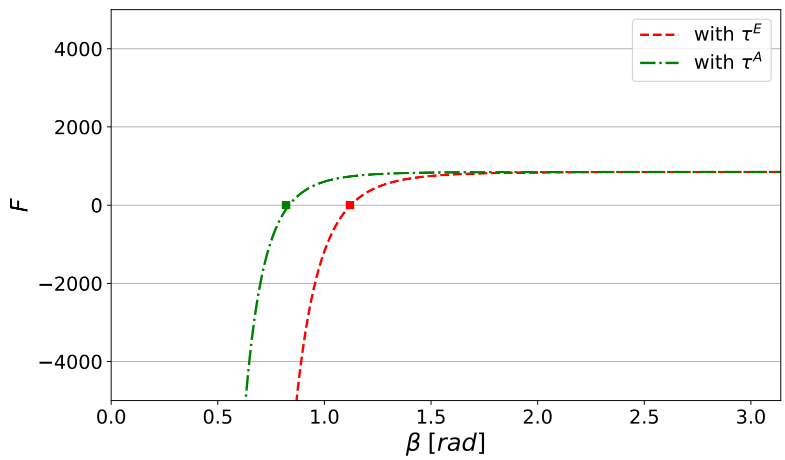

Figure 18: Net of momentum (F) (Eq. 28) calculated using τ^E (red dashed, Eqs. 29 - 30) and τ^A (green dot-dashed, Eqs. 21 - 22) for air-water two-phase flow in 3RFL with d=69.85 mm, D = 0.84 m, $\varphi_L = 0.05$, $\theta = 5°$ and $f_R = 11.23$ opm. Filled squares mark the condition $F = 0$.

flat interface sketched in Fig. 17, the potential energy per unit length of the pipe is given as the sum of the potential energies of air and water phases:

$$E_P = E_{P_G} + E_{P_L} = A_L \rho_L g h_{cL} \cos\theta + A_G \rho_G g h_{cG} \cos\theta \tag{34}$$

where h_{cG} and h_{cL} are gas and liquid phases' gravity centres considered as: (Sharma et al., 2011):

$$h_{cG} = r\left[1 + \frac{4}{3}\frac{\sin^3(\frac{\beta}{2})}{2\pi - \beta + \sin\beta}\right] \qquad h_{cL} = r\left[1 - \frac{4}{3}\frac{\sin^3(\frac{\beta}{2})}{\beta - \sin\beta}\right] \tag{35}$$

Analogously, the kinetic energy of the system per unit length of the pipe is the sum of the kinetic energies of air and water phases:

$$E_K = E_{K_L} + E_{K_G} = \frac{1}{2} A_L \rho_L U_L^2 + \frac{1}{2} A_G \rho_G U_G^2 \tag{36}$$

The surface energy of the two-phase flow per unit length of the pipe combines the surface energies at the gas-wall, liquid-wall and gas-liquid interfaces, considering that the latter is flat:

$$E_S = E_{S_{WL}} + E_{S_{GL}} + E_{S_{WG}} = S_L \sigma_{WL} + S_I \sigma_{GL} + S_G \sigma_{WG} \tag{37}$$

Here, σ_{WG}, σ_{GL} and σ_{WL} are wall-gas, gas-liquid and wall-liquid surface tensions (σ_{GL} = 72.8 mN/m (Vargaftik et al., 1983), σ_{WL}= 34 mN/m (Schilling et al., 2010)), respectively . The wall-gas surface tension σ_{WG} is neglected. The total energy of the system per unit length of the pipe reads:

$$E_T = E_K + E_P + E_S \tag{38}$$

According to the energetic understanding of the problem, the solution of the system is the β resulting in the minimum total energy $E_{T_{min}}$, *i.e.* $\beta_{min} = \beta(E_{T_{min}})$.

Fig. 19 displays the variations in the total energy of the system (Eq. 38) depending on the hydraulic angle. Here, the filled circle identifies the solution corresponding to the minimum of the total energy. The resulting hydraulic angle can be expressed in terms of the liquid height using the Eq. 1.

It is worth mentioning that the total energy of the system as a function of hydraulic angle exhibits a table-top behaviour around the local minimum. Thus, we have defined a region represented by the rectangle in Fig. 19, delimited by two values of β, *i.e.* β_{low} and β_{high}, for which $\beta_{low} < \beta < \beta_{high}$. These values of β correspond to the hydraulic angle for which E_T varies by 25% concerning to its minimum. Once the ranges of the table-top region are specified, the extreme values of the hydraulic angles, are expressed in terms of the liquid height and compared to experimental results in section 4.4.

4.3. Combined Approach

In this section, we bring together the mechanistic approach along with the energy minimization concept. Assuming the continuity of the pressure gradient in the gas and in the liquid phase, and summing up the separate momentum equations (24) and (25), one can derive the total pressure gradient per unit length of the tube:

$$\frac{dP}{dx} = g \sin\theta(\rho_L \frac{A_L}{A_T} + \rho_G \frac{A_G}{A_T}) - \tau_{WL}\frac{S_L}{A_T} - \tau_{WG}\frac{S_G}{A_T} \tag{39}$$

One of the benefits of this mathematical operation is the liberation of the combined momentum equation (39) from the shear stress at the interface τ_I, whose closure is usually a source of error. In order to combine the mechanistic and energetic models, we follow Herri et al. (2017), where the authors minimized the product of pressure gradient (Eq. 39) by the total energy of the system (Eq. 38):

$$min|\frac{dP}{dx}E_T| \tag{40}$$

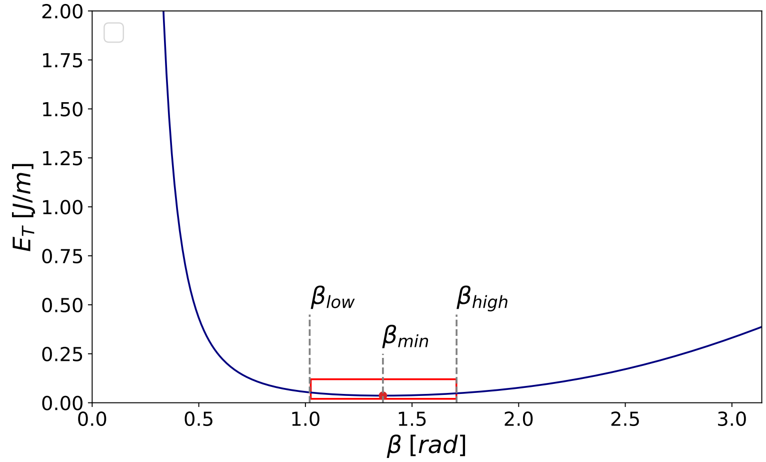

Figure 19: Total energy of air-water two-phase flow in 3RFL with d=69.85 mm, $D = 0.84$ m, $\varphi_L = 0.05$, $\theta = 5°$ and $f_R = 11.23$ opm. The filled red circle marks the total energy's local minimum $E_{T_{min}}$. The red rectangle identifies the table-top behaviour around the local minimum (β_{min}) of the $E_T = f(\beta)$ function, where β_{high} and β_{low} identify the high and low limits.

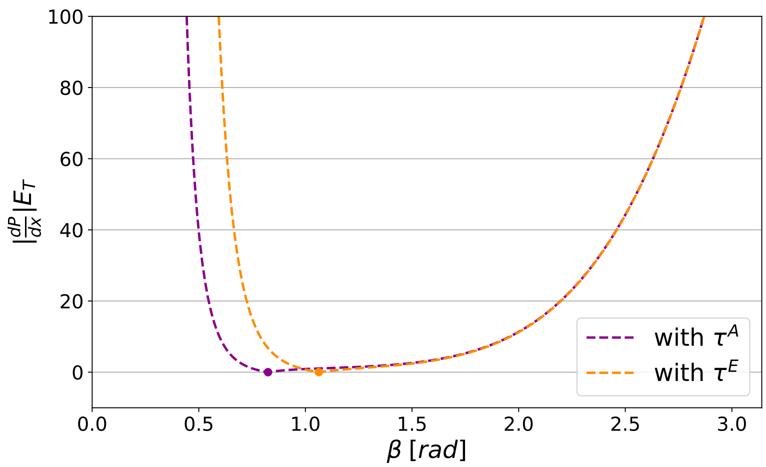

Figure 20: The product of pressure gradient exerted on the conduit cross section (Eq. 39) by the total energy of the system (Eq. 38) calculated using τ^E (orange dashed) and τ^A (purple dashed) shear stresses. Filled circles identify the local minima.

Fig. 20 presents the product of the pressure gradient by the total energy of the system as a function of β. Two approaches are employed to compute τ_{WG} and τ_{WL} in the Eq. (16): the empirical correlations τ^E (Eqs. 29 - 30), and the analytical expressions τ^A (Eqs. 21 - 22). The hydraulic angle corresponding to the local minimum (marked with filled circles) is recovered and expressed in terms of the liquid height following Eq. 1. Combined approach predictions are compared to the experimental measurements in the following section.

4.4. Comparison between experimental and modelling results

Fig. 21 shows the average liquid height $\overline{h}_L$ as a function of the rocking rate f_R, and compares experimental results (black circles) and model predictions. The chosen configuration is: $d = 69.85$ mm, $\varphi_L = 0.05$, $\theta = 5°$ and air-water flow. The boundaries of corresponding flow regimes are defined by vertical lines, as observed experimentally. Both mechanistic and combined model predictions are evaluated using for the wall shear stress empirical correlations τ^E (Eqs. 29 - 30) and analytical expressions τ^A (Eqs. 21 - 22). When employing the analytical correlation τ^A for the shear stress, the predicted liquid height is underestimated for both the mechanistic (green solid line) and the combined (orange dot-dashed line) models, with respect to the scenario where τ^E is instead used, *i.e.* red solid line (mechanistic model) and purple dot-dashed line (combined model). Meanwhile, combined approach predictions employing τ^E (τ^A) situate close to the predictions of the mechanistic model employing τ^E (τ^A), suggesting that the choice of the shear stress modeling plays an important role in the liquid film height prediction, even more than the choice of the modeling strategy itself (mechanistic or combined). However, the total energy minimization model (blue solid line), which by construction disregards the shear stress, provides an overestimation of the liquid film height predictions with respect to the mechanistic and combined approaches, regardless of the choice of the shear stress modeling. Nonetheless, when considering the confidence range of solutions (blue dotted lines) defined by the table-top region shown in Fig. 19, the lower limit predicts liquid film heights close to those of the mechanistic and combined approaches using τ^E.

The discrepancy observed between experimental results and mechanistic or combined models in the smooth interrupted (SI) and wavy-bubbly continuous (WBC) flow regimes can be attributed to the inconsistency between the modeling assumption of stratified flow with flat interface and the actual characteristics of the flow. Indeed, the SI and WBC regimes typically exhibit

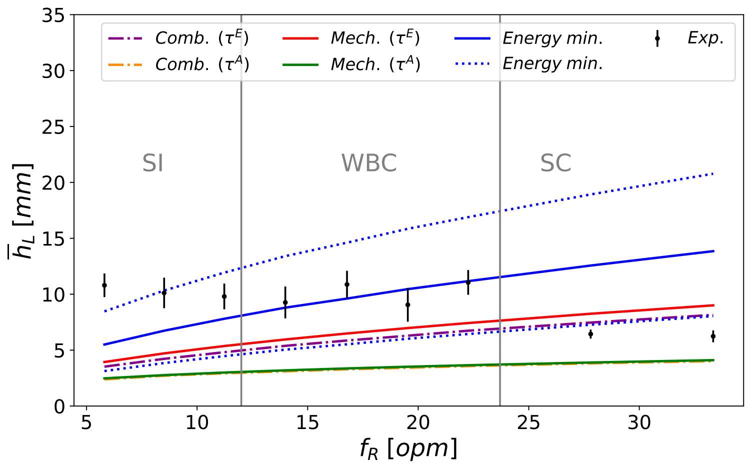

Figure 21: A comparison between liquid height predictions obtained from models, *i.e.* the mechanistic model with τ^A (green line) and τ^E (red line), energy minimization model (blue line) with the confidence range (blue dotted line), combined model with τ^A (purple dot-dashed line) and τ^E (orange dot-dashed line) and experimental results (black circles) considering air-water flow in the 3RFL with d=69.85 mm, φ_L=0.05, θ=5° and various rocking rates.

a hump-shaped distribution of liquid along the flow (table 4). In contrast, the smooth continuous (SC) regime, characterized by its wall-clinging effect that promotes smooth interface and uniform distribution of liquid around the tube, matches more with the above-mentioned modeling assumption. Hence, experimental results for the SC regime align closely with mechanistic and combined models predictions. Finally, we can conclude that the total energy minimization model best predicts the experimental liquid heights, in particular for the wavy-bubbly continuous flow. In addition, if confidence range is considered (blue dotted line), the liquid height predictions remain within the range of error bars for the all the experimental points, except the two limiting ones (very low and very large rocking frequency). However, noteworthy is that while the experimental liquid height is a constant or slightly decreasing function of the rocking frequency, the total energy minimization model - and also the mechanistic and the combined approach - predicts a growing trend of $\overline{h}_L$ with f_R. This suggests that there is room for future improvements in the modeling strategy.

5. Conclusions

In conclusion, we have presented a new experimental system, the Rocking and Rolling Ring Flow Loop, which can achieve controlled atmospheric flow and different flow regimes. The advantages of the 3RFL are the simplicity of fabrication, along with fast and simple operation and an accessible interior. Besides, the geometry of the test section allows replicating flowlines of any length. Another strength of the apparatus is flow initiation using mechanical motion, rather than using pumping systems.

The transparency of the test section allowed flow regime analysis. For the studied control parameters range, three flow regimes were identified, such as smooth interrupted, smooth continuous and wavy-bubbly continuous (Fig. 10). Air-water flow behaviour in the 3RFL showed similarities with flow through the coiled tubes in terms of asymmetry of the flow in the radial direction (for SC and WBC flow regimes), non-homogeneous air bubbles distribution along the flow (for WBC flow) and wall-clinging effect (for SC flow). Given that coiled tubes can be used for heat-exchange applications, natural gas hydrates separation from wax and asphaltenes (Tian et al., 2022), and food and drugs manufacturing, flow regimes characterization presented in the current work enriches experimental data on this matter. Flow observations were arranged into flow regime maps to evaluate flow regime transition criteria and the impact of system control parameters on the emergence of particular flow regimes (Fig. 11). It was found that flow regime transitions are mainly attributed to the value of the Fr number. Given that Fr expresses the ratio of centrifugal forces to gravity, we conclude that competition between these two effects gives the resulting flow regime (Fig. 12).

Three models were selected to predict the average liquid height of the air-water flow in the 3RFL: mechanistic, total energy minimization and a combined approach. Analytical expressions for the shear stress were developed from the velocity profiles of liquid and gas. These expressions have been employed as closure relations in the modeling approaches, and the resulting liquid height have been compared to the case of empirical shear stress correlations. Among those three employed modeling strategies, we have found that the total energy minimization model best compares to the experimental liquid height (Fig. 21).

Future work will concentrate on the parallel evolution of the complexity of the experimental system and modeling. Improvements in experimental research will involve advancing the experimental setup by introducing additional elements such as the oil phase and/or solid particles, implementing pressurization, and establishing temperature control. These enhancements will enable the development of a multi-instrumental flow loop for crystallization experiments.

References

Akagawa, K., Kono, M., Sakaguchi, T., Nishimura, M., 1971. Study on distribution of flow rates and flow stabilities in parallel long evaporators. Bulletin of JSME 14, 837–848.

Amaravadi, S., 1994. The effect of pressure on two-phase zero-net liquid flow in inclined pipes, in: SPE Annual Technical Conference and Exhibition, OnePetro.

Balakin, B.V., 2010. Experimental and theoretical study of the flow, aggregation and deposition of gas hydrate particles. Doctoral Dissertation, The University of Bergen .

Banerjee, S., Rhodes, E., Scott, D.S., 1969. Studies on cocurrent gas-liquid flow in helically coiled tubes. i. flow patterns, pressure drop and holdup. The Canadian Journal of Chemical Engineering 47, 445–453.

Barnea, D., Taitel, Y., 1992. Structural and interfacial stability of multiple solutions for stratified flow. International journal of multiphase flow 18, 821–830.

Barnea, D., Taitel, Y., 1994. Interfacial and structural stability of separated flow. International journal of multiphase flow 20, 387–414.

Blasius, H., 1913. Das aehnlichkeitsgesetz bei reibungsvorgängen in flüssigkeiten, in: Mitteilungen über Forschungsarbeiten auf dem Gebiete des Ingenieurwesens. Springer, pp. 1–41.

Chakrabarti, D.P., Das, G., Ray, S., 2005. Pressure drop in liquid-liquid two phase horizontal flow: Experiment and prediction. Chemical Engineering & Technology 28, 1003–1009.

De Almeida, V., Serris, E., Lavalle, G., Cameirão, A., Herri, J.M., Abadie, E., Lesage, N., Fidel Dufour, A., 2023. Mechanisms of hydrate blockage in oil-water dispersions based on flow loop experiments. Chemical Engineering Science 273, 118632.

Dean, W.R., 1927. Xvi. note on the motion of fluid in a curved pipe. The London, Edinburgh, and Dublin Philosophical Magazine and Journal of Science 4, 208–223.

Eustice, J., 1911. Experiments on stream-line motion in curved pipes. Proceedings of the Royal Society of London. Series A, Containing Papers of a Mathematical and Physical Character 85, 119–131.

Fidel-Dufour, A., Gruy, F., Herri, J., 2005. Experimental characterization and modelling of the rheological properties of methane hydrate slurries during their crystallisation in a water in dodecane emulsion under laminar flowing. Chemical Engineering Science 61, 505–515.

Garcıa, F., Garcıa, R., Padrino, J., Mata, C., Trallero, J., Joseph, D., 2003. Power law and composite power law friction factor correlations for laminar and turbulent gas-liquid flow in horizontal pipelines. International Journal of Multiphase Flow 29, 1605–1624.

Herri, J.M., Sum, A.K., Cameirao, A.A., Bouillot, B., 2017. Modeling non-equilibrium crystallization of gas hydrates under stratified flow conditions, in: 9 th International Conference on Gas Hydrates-ICGH9.

Kaji, M., Nakanishi, S., Mori, K., Kume, M., Moriya, T., 1984. Study on dryout in helically coiled steam generating tubes, 1. comparison of experimental results between coiled and straight tubes. Japan 50.

Kelland, M.A., Grinrød, A., Dirdal, E.G., 2015. Novel benchtop wheel loop for low dosage gas hydrate inhibitor screening: comparison to rocking cells for a series of antiagglomerants. Journal of Chemical & Engineering Data 60, 252–257.

Kinnari, K., Hundseid, J., Li, X., Askvik, K.M., 2015. Hydrate management in practice. Journal of Chemical & Engineering Data 60, 437–446.

Kinnari, K., Labes-Carrier, C., Lunde, K., Hemmingsen, P.V., Davies, S.R., Boxall, J.A., Koh, C.A., Sloan, E.D., 2008. Hydrate plug formation prediction tool–an increasing need for flow assurance in the oil industry. In: Proceedings of the 6th International Conference on Gas Hydrates (ICGH 2008) .

Landman, M.J., 1991. Non-unique holdup and pressure drop in two-phase stratified inclined pipe flow. International journal of multiphase flow 17, 377–394.

Lee, H., Al-Sarkhi, A., Pereyra, E., Sarica, C., Park, C., Kang, J., Choi, J., 2013. Hydrodynamics model for gas–liquid stratified flow in horizontal pipes using minimum dissipated energy concept. Journal of Petroleum Science and Engineering 108, 336–341.

Melchuna, A.M., 2016. Experimental study and modeling of methane hydrates cristallization under flow from emulsions with variable fraction of water and anti-agglomerant. Ph.D. thesis. Doctoral dissertation, Université de Lyon.

Murai, Y., Yoshikawa, S., Toda, S.i., Ishikawa, M.a., Yamamoto, F., 2006. Structure of air–water two-phase flow in helically coiled tubes. Nuclear engineering and design 236, 94–106.

Nusselt, W., 1916. Die oberflachenkondensation des wasserdamphes. VDI-Zs 60, 541.

Ouyang, L.B., Aziz, K., 1996. Steady-state gas flow in pipes. Journal of Petroleum Science and Engineering 14, 137–158.

Pham, T.K., Cameirao, A., Melchuna, A., Herri, J.M., Glénat, P., 2020. Relative pressure drop model for hydrate formation and transportability in flowlines in high water cut systems. Energies 13, 686.

Sa, J.H., Melchuna, A., Zhang, X., Morales, R., Cameirao, A., Herri, J.M., Sum, A.K., 2019. Rock-flow cell: an innovative benchtop testing tool for flow assurance studies. Industrial & Engineering Chemistry Research 58, 8544–8552.

Schilling, M., Bouchard, M., Khanjian, H., Learner, T., Phenix, A., Rivenc, R., 2010. Application of chemical and thermal analysis methods for studying cellulose ester plastics. Accounts of chemical research 43, 888–896.

Sharma, A., Al-Sarkhi, A., Sarica, C., Zhang, H.Q., 2011. Modeling of oil–water flow using energy minimization concept. International Journal of Multiphase Flow 37, 326–335.

Sum, A.K., Koh, C.A., Sloan, E.D., 2009. Clathrate hydrates: From laboratory science to engineering practice. Industrial & Engineering Chemistry Research 48, 7457–7465.

Taitel, Y., Barnea, D., 1990. Two-phase slug flow. Advances in heat transfer 20, 83–132.

Taitel, Y., Dukler, A.E., 1976a. A model for predicting flow regime transitions in horizontal and near horizontal gas-liquid flow. AIChE journal 22, 47–55.

Taitel, Y., Dukler, A.E., 1976b. A model for predicting flow regime transitions in horizontal and near horizontal gas-liquid flow. AIChE journal 22, 47–55.

ISO/IEC, 2008. Uncertainty of measurement — Part 3: Guide to the expression of uncertainty in measurement (GUM:1995) . 2008(E) ed., International Organization for Standardization, Geneva, Switzerland. URL: https://www.iso.org/standard/50461.html.

Thibault, D., Munoz, J.M., Liné, A., 2015. Multiple holdup solutions in laminar stratified flow in inclined channels. International Journal of Multiphase Flow 73, 275–288.

Tian, J., Xiao, X., Yang, L., Liu, C., Guo, L., 2022. Separation mechanism and dynamics characteristics of natural gas hydrate by helically coiled tube. Heat and Mass Transfer 58, 1459–1471.

Ullmann, A., Zamir, M., Gat, S., Brauner, N., 2003. Multi-holdups in co-current stratified flow in inclined tubes. International journal of multiphase flow 29, 1565–1581.

Vargaftik, N., Volkov, B., Voljak, L., 1983. International tables of the surface tension of water. Journal of Physical and Chemical Reference Data 12.

Xiao, J., Shonham, O., Brill, J., 1990. A comprehensive mechanistic model for two-phase flow in pipelines, in: SPE Annual Technical Conference and Exhibition, OnePetro.

Zhu, G., Yang, X., Jiang, S., Zhu, H., 2019. Intermittent gas-liquid two-phase flow in helically coiled tubes. International Journal of Multiphase Flow 116, 113–124.